

Kennesaw State University

DigitalCommons@Kennesaw State University

---

Master of Science in Chemical Sciences Theses

Department of Chemistry and Biochemistry


---

Summer 7-22-2021

## Desorption of Non-Exchangeable Radiocesium in soil from Fukushima Prefecture, Japan

Grayson Phillips

Follow this and additional works at: [https://digitalcommons.kennesaw.edu/mscs\\_etd](https://digitalcommons.kennesaw.edu/mscs_etd)

 Part of the [Analytical Chemistry Commons](#), [Environmental Chemistry Commons](#), [Inorganic Chemistry Commons](#), and the [Other Environmental Sciences Commons](#)

---

### Recommended Citation

Phillips, Grayson, "Desorption of Non-Exchangeable Radiocesium in soil from Fukushima Prefecture, Japan" (2021). *Master of Science in Chemical Sciences Theses*. 42.  
[https://digitalcommons.kennesaw.edu/mscs\\_etd/42](https://digitalcommons.kennesaw.edu/mscs_etd/42)

This Thesis is brought to you for free and open access by the Department of Chemistry and Biochemistry at DigitalCommons@Kennesaw State University. It has been accepted for inclusion in Master of Science in Chemical Sciences Theses by an authorized administrator of DigitalCommons@Kennesaw State University. For more information, please contact [digitalcommons@kennesaw.edu](mailto:digitalcommons@kennesaw.edu).

Desorption of Non-Exchangeable Radiocesium in soil from Fukushima Prefecture, Japan

by

Grayson Phillips

M.S. Chemistry

Kennesaw State University, 2021

---

Submitted in Partial Fulfillment of the Requirements

For the Degree of Master of Science in the

Department of Chemistry and Biochemistry

Kennesaw State University

July 2021

DocuSigned by:  
*Daniel Ferreira*  
1AC764AB1A604C8...

Committee Chair

DocuSigned by:  
*Bharat Baruah*  
E72DF8FDD75F433...

Committee Member

DocuSigned by:  
*Altug Payraz*  
70C492D048FB477...

Committee Member

DocuSigned by:  
*Chris Sockery*  
C1295244895A414...

Graduate Program Coordinator

DocuSigned by:  
*Mark Mitchell*  
68C4A21FAB064E5...

Department Chair

DocuSigned by:  
*Kojo Mensa-Wilmot*  
39226A8692FB45B...

College Dean



## ACKNOWLEDGMENTS

Drs. Daniel Ferreira and Bharat Baruah for all the support and guidance

Derek McNutt, Nathan Boon, and Victoria Romero for their laboratory input and  
experimental help

Kennesaw State University's Department of Chemistry and Biochemistry for providing  
me with this opportunity

My Wife Victoria Phillips for her constant support and encouragement

My parents Drs. Cyndee and David Phillips and my grandparents Emily and Calvin  
Phillips for instilling in me my love of science and education

## ABSTRACT

The Fukushima Daiichi Nuclear Powerplant was struck by an earthquake and a tsunami resulting in the meltdown of four of the six reactor cores operating at the plant. As a result, nuclear waste was released from the plant, contaminating the soil in the region. Most of the contamination was sequestered within the few inches of the soil but unluckily the contamination, radiocesium formed a non-exchangeable bond. The Japanese government bagged this soil and has stored it in fields surrounding the exclusion zone. Long-term storage facilities have not been determined. This is a study of the available resources to determine if, in fact, the soil can be chemically treated to the point that it can be stored in a normal hazardous waste facility. The study proposes to utilize a ligand to capture the cesium with a higher binding affinity and remove it from the equilibrium by precipitation possibly forcing the exchange of the “non-exchangeable” ion.

## TABLE OF CONTENTS

ACKNOWLEDGMENTS .....	ii
ABSTRACT.....	iii
LIST OF TABLES/LIST OF FIGURES .....	vi
LIST OF KEY ACRONYMS.....	viii
CHAPTER 1. INTRODUCTION .....	1
1.1 Background of Fukushima Disaster.....	1
1.2 Deposition of Cs <sup>+</sup> in the Top Soil and how it Becomes Non-exchangeable.....	3
1.3 Decay of Cs <sup>+</sup> and Health Concerns .....	5
1.4 Government Response to the Disaster .....	6
CHAPTER 2. Understanding Cs <sup>+</sup> Adsorption Envelopes .....	8
2.1 The NISE effect and adsorption envelope studies .....	8
2.2 Materials and Methods .....	10
2.3 Results and Discussion .....	13
CHAPTER 3. Comparing Selective Precipitation Agents .....	20
3.1 Introduction.....	20
3.2 Materials and Methods.....	23
3.3 Synthesis of H <sub>5</sub> PMo <sub>10</sub> V <sub>2</sub> O <sub>40</sub> (MVPA) .....	25

3.4 Synthesis of H <sub>4</sub> SiW <sub>12</sub> O <sub>40</sub> (STA) .....	23
3.5 Characterization and Spectroscopy .....	24
3.6 ICP Measurements .....	24
3.7 Understanding Speciation of POMs and Stiochiometry of POMs and TFPB .....	24
3.8POM Precipitation Controls.....	25
3.9 Results and Discussion .....	25
CHAPTER 4. Forced Precipitation of Non-Exchangable Cs in Pure Phase Vermiculite.	36
4.1 Introduction.....	36
4.2 Materials and Method .....	38
4.3 Results.....	41
CHAPTER 5. Rem Method for Fukushima Soil .....	47
5.1 Improvements & Optimal Conditions.....	47
5.2 Concerns and Limitations .....	48
5.3 Conclusion .....	49
REFERENCES .....	50

## LIST OF TABLES/LIST OF FIGURES

<u>FIGURE 1.1 Damage at FDNPP</u> .....	1
<u>FIGURE 1.2 Map of exclusion zone</u> .....	2
<u>FIGURE 1.3 Schematic representing Cs<sup>+</sup> adsorption on vermiculite</u> .....	5
<u>FIGURE 1.4 Image of bagged fukushima soil</u> .....	7
<u>FIGURE 2.1 Adsorption envelope for Cs<sup>+</sup> on vermiculite</u> .....	9
<u>TABLE 2.1 Parameters for models of Cs<sup>+</sup> adsorption</u> .....	12
<u>TABLE 2.2 Properties of zeolite minerals</u> .....	13
<u>TABLE 2.3 Characteristics of monovalent ions</u> .....	14
<u>FIGURE 2.2 An adsorption envelope for Cs<sup>+</sup> on Zeolite Y</u> .....	15
<u>FIGURE 2.3 An adsorption envelope for Cs<sup>+</sup> on ZSM-5</u> .....	16
<u>FIGURE 2.4 An adsorption envelope for Cs<sup>+</sup> on Ferrierite</u> .....	16
<u>FIGURE 2.5 Adsorption envelopes for Na<sup>+</sup> on zeolite minerals</u> .....	17
<u>FIGURE 3.1 Molecular structures of Keggin type POMs</u> .....	22
<u>Scheme 3.1 Proposed selective precipitation formation phenomenon</u> .....	22
<u>FIGURE 3.2 FTIR spectra of POMs</u> .....	27
<u>TABLE 3.1 FTIR signal assignments of POMs and POM-Cs compounds</u> .....	27
<u>FIGURE 3.4 Raman spectra of POMs</u> .....	28
<u>FIGURE 3.5 UV-vis spectra of POMs</u> .....	29
<u>FIGURE 3.6 XRPD plots for POMs</u> .....	30
<u>FIGURE 3.7 MVPA extraction as a function of pH</u> .....	31



<u>FIGURE 3.8 PTA extraction as a function of pH</u> .....	32
<u>FIGURE 3.9 TFPB extraction as a function of pH</u> .....	32
<u>TABLE 3.2 POM extraction Stoichiometry Results</u> .....	34
<u>FIGURE 4.1 Graph of Cs<sup>+</sup> extraction from pure phase vermiculite using TFPB</u> .....	42
<u>FIGURE 4.2 Graph of Cs<sup>+</sup> extraction from pure phase vermiculite using PTA</u> .....	43
<u>FIGURE 4.3 Graph of Cs<sup>+</sup> extraction from pure phase vermiculite using MVPA</u> .....	44
<u>FIGURE 4.4 Graph of Cs<sup>+</sup> extraction from pure phase vermiculite using STA</u> .....	45

## LIST OF KEY ACRONYMS

Fukushima Daiichi Nuclear Power Plant: FDNPP

Special Decontamination Zone: SDZs

Intensive Contamination Survey Area: ICA

Inductively Coupled Plasma – Optical Emission Spectrum: ICP-OES or ICP

Nanopore Inner-Sphere Enhancement: NISE

polyoxometalate: POM

Phosphotungstic acid: PTA

Molybdovanadophosphoric acid: MVPA

Silicotungstic acid: STA

Tetrakis (4-fluorophenyl) borate: TFPB

Fourier-transform infrared spectroscopy: FTIR

X-ray powder diffraction: XRPD

## CHAPTER 1 INTRODUCTION

### *1.1 Background of Fukushima Disaster*

On March 11, 2011, the Great Tōhoku earthquake took place about 130km off the coast of Japan at a depth of about 30km under the ocean floor. This earthquake was responsible for the damage itself and created several tsunamis which caused the mass destruction of many coastal cities. Many cities were literally swept away.



**Figure 1.1** Damage at Fukushima Daiichi Nuclear Power Plant, run by Tokyo Electric Power Co.—Kyodo News/AP

The earthquake severely damaged the Fukushima Daiichi Nuclear Power Plant (FDNPP). One of the tsunamis resulted in the meltdown of four of the six reactor cores operating at the plant. This nuclear disaster marks the worst nuclear accident since the Chernobyl disaster in 1986. Four days

after the disaster, radionuclide laced particles were ejected in the smoke plume from the nuclear reactors into the upper atmosphere. These then settled across the landscape covering a large area (See Figure 1.1).

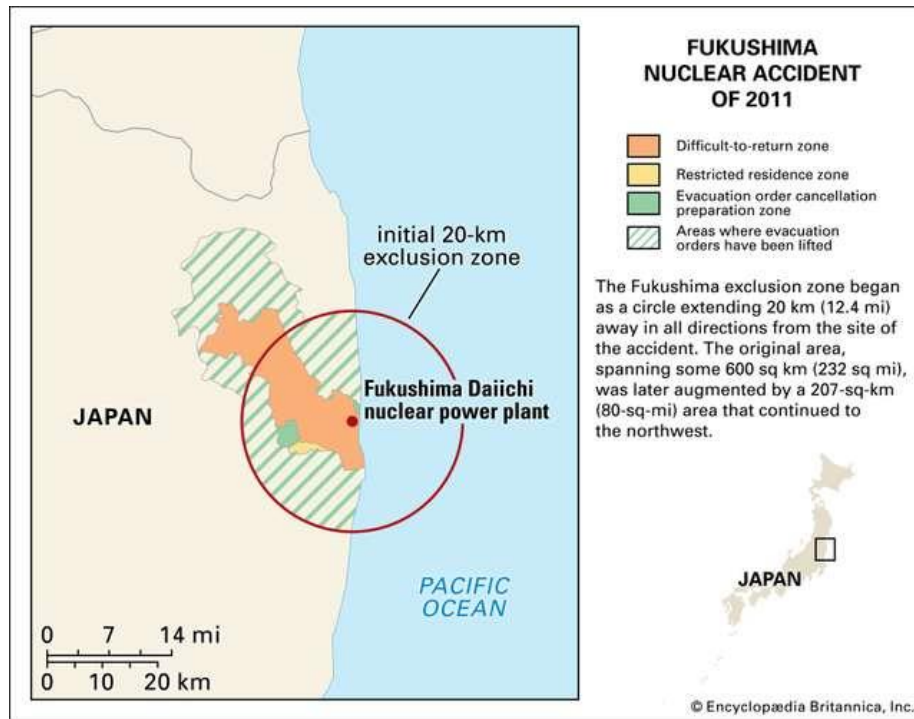


**Figure 2.2** Map of exclusion zone set up by Japanese government. – Encyclopedia Britannica, inc.

The earthquake significantly damaged three of the reactor cores, but the disastrous effects of this incident multiplied when the tsunami disabled the back-up cooling system and its generators. This led to an explosion in three of the reactor buildings due to the ignition of excess hydrogen gas. The explosion and the following fire ejected huge quantities of radionuclide laced particles into the atmosphere. Most of this contamination was dispersed into water, since cesium is generally very soluble, but because the soil in the Fukushima Prefecture contains a high percentage of vermiculite in the clay fraction, the topsoil retained a high concentration of radioactive cesium ( $^{137}\text{Cs}$ ).<sup>1,2</sup>

## *1.2 Deposition of Cs into the topsoil and how it becomes nonexchangeable.*

Initial studies found that the  $^{137}\text{Cs}$  was able to become non-exchangeable within the interlayer of the vermiculite clay. Cesium becomes non-exchangeable when adsorbed into the interlayers of 2:1 clays like vermiculite, and some other similar clays in the surface of the soil around Fukushima similarly to the non-exchangeable adsorption of potassium ( $\text{K}^+$ ) in mica.<sup>3-12</sup> Potassium adsorption into 2:1 clays causes a phenomenon called interlayer collapse, meaning the interlayers of the clay collapse around the  $\text{K}^+$  effectively trapping it within the clay structure. The chemistry of clay structures must be understood first in order to hypothesize the effects of non-exchangeable adsorption.

There are many types of clays that have unique properties, which affect the structure of the clay and adsorption properties. For example, whether they swell or shrink when dehydrated or exposed to water, whether their cations are exchangeable and to what degree they are interchangeable. The best way to begin characterizing clay is to think about it in terms of its simple repeating structures and what conformation they take.<sup>13</sup> The basic building blocks of clay are repeated crystal sheets that are either octahedral or tetrahedral. These sheets interact with each other to form the layers of the clay. With the help of adsorbed cations, the layers of clay form the crystal structure of the clay. Silicate clays are the most common type of clays on earth. They exist either as 1:1 clay or 2:1 clay. What these numbers reference is the composition of the layer of the clay. In silicate clays there are tetrahedral sheets, and octahedral sheets. The tetrahedral sheets are a repeating series of silicon atoms surrounded by 4 oxygen atoms each.<sup>13</sup> Octahedral sheets are usually aluminum, oxygen and hydroxides. The aluminum will have 6 oxygen atoms associated with it regardless of whether they are hydroxides or not. A 2:1 clay has two tetrahedral sheets and one octahedral sheet, a 1:1 clay is one tetrahedral sheet and one octahedral sheet, per layer.<sup>13</sup> The interlayers of the clay crystal

structure are usually negatively charged. This is because of a process in the development of the clay called isomorphous substitution. Isomorphous substitution occurs when cations with a lower charge are substituted for aluminum or silicon in the crystal sheets.<sup>13</sup> Some of the oxygens in the crystal structure carry a negative charge that attracts cations from the soil solution to satisfy the charge imbalance in the clay. These cations are an important part of the repeating crystal structure of the clay because tetrahedral sheets will naturally repel from each other but are held together by the cation interactions. At the atomic level the surfaces of the interlayers are not smooth but are marked with large quantities of ditrigonal siloxane cavities. These cavities give the interlayer the appearance of two egg crates facing one another. In vermiculite the ditrigonal siloxane cavities have a radius of 2.6 Å. The Cs<sup>+</sup> ion has an atomic radius of ~1.8 Å.<sup>14</sup> This tight fit helps explain why the adsorption of Cs<sup>+</sup> into the vermiculite interlayers is so strong, being nearly fully encapsulated within the cavity (Figure 1). The Cs<sup>+</sup> adsorption within the interlayer mechanistically uses inner-sphere adsorption which is much stronger than other types of adsorption.<sup>15,16</sup> Once the interlayer collapse occurs with the strong inner-sphere adsorption mechanism, the ion effectively becomes a glue holding the interlayer shut. This phenomenon prevents expansion and traps the adsorbed Cs<sup>+</sup> inside the interlayer. It has been shown that Cs<sup>+</sup> seals the interlayer even more tightly than K<sup>+</sup> does in micas.<sup>17</sup>

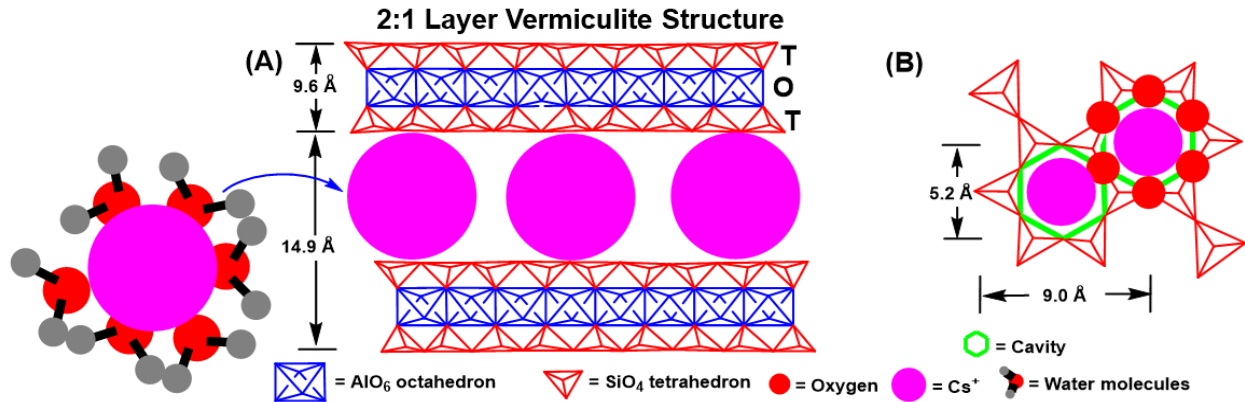


**Figure 1.3** Schematic representation of Cs<sup>+</sup> adsorbing on vermiculite, (A) side view of Cs<sup>+</sup> dehydrating as it moves from the bulk solution to adsorb in the vermiculite interlayer and collapse it; and (B) top view of one ditrigonal siloxane cavity with Cs<sup>+</sup> ion surrounded by O atoms of tetrahedral layer.<sup>18,19</sup> (Figure from A Comparison of Cesium adsorption on Zeolite Minerals to Vermiculite Clay, Ferreira, Phillips, and Baruah, 2020 Submitted to Clay and Clay minerals)

### 1.3 Decay of Cs and Health Concerns

One of the most apparent concerns surrounding any radioactive contamination is possible health effects related to the decay of the radioactive materials. This risk also represents the main incentive behind decontaminating the area after a nuclear disaster. It is well known that exposure to radioactive material can lead to long term health effects, and exposure to high radiation levels can lead to immediate death. The principal contaminants from the Fukushima Daiichi Nuclear Power Plant disaster were <sup>137</sup>Cs and <sup>134</sup>Cs. Ten years after the disaster most of the <sup>134</sup>Cs has become its decay product <sup>134</sup>Ba. This leaves only the more dangerous <sup>137</sup>Cs, which is a gamma emitter during its decay process and has a half-life of ~ 30 years as it decays into <sup>137</sup>Ba.<sup>20</sup> This makes the contaminant much more dangerous both in the short term and the long term compared to <sup>137</sup>Cs (half-life of ~1 year) and could lead to serious health complications for people living in the area. When considering the health effects of exposure to radioactive material both annual dose, and single-dose exposure must be considered. Some of the decontamination workers who worked in

areas with the highest concentration of waste were studied for exposure, their bodies were scanned for internal (inhalation) exposure for both  $^{134}\text{Cs}$  and  $^{137}\text{Cs}$ , the levels in their bodies were non-detectable by the equipment used at the study (detection limit 300 bq.<sup>21,22</sup> There have also been studies examining the environment of the people who have returned to living in the Intensive Contamination Survey Area (ICAs) which have less contamination than the Special Decontamination Zones (SDZs). However, the ICAs have almost ten times the population of the SDZs making this region a more important survey area for the health effects of this contamination. The people living in the ICAs are exposed to 1-5 mSv  $^{-\text{yr}}$  which is about the same as receiving a mammogram.<sup>23,24</sup> It is important to note this low yearly dose is after decontamination efforts from the government.

#### *1.4 Government Response to the Disaster*

After the incident, the affected area where the radiation levels were above safe concentrations were labeled as an exclusion zone and citizens were evacuated. After the area was clear, the government removed the top layer of soil (where the radiocesium was sequestered) and stored it in bags.<sup>1</sup> The immediate storage plan at the time was to concentrate the bagged waste in specific locations (abandoned fields) in Fukushima Prefecture. Since then, short-term storage facilities have been constructed, but no long-term storage plans have been finalized for this soil, which amounts to more than 15 million cubic meters of material.<sup>25</sup>





**Figure 1.4** Image of bagged Fukushima soil in field, Fukushima Prefecture, Japan. Photo by Dr. Ferreira

## **CHAPTER 2. UNDERSTANDING Cs<sup>+</sup> ADSORPTION ENVELOPES**

### *2.1 The NISE effect and adsorption envelope studies*

Adsorption envelope studies are commonly used to characterize an ion's adsorption onto a mineral surface and can be used to compare an ion's affinity for adsorption on different minerals; or other ions on the same mineral.<sup>26-35</sup> Zeolite minerals consist of aluminosilicate units that form crystal structures. Depending on the conformation different nanopore channels form. These nanopores channels cause zeolites to have very large surface areas, which makes them valuable for chemical reactions, acting as molecular sieves, separation membranes, catalysts, or photochemical hosts.<sup>36</sup> Currently there are 241 (50 natural and 191 synthetic) unique zeolite minerals that have been discovered. Each of these zeolites have a unique crystal structure and form nanopores of different diameters.<sup>37,38</sup> Because of the nano-porosity of zeolites they are extremely effective at demonstrating the Nanopore Inner-Sphere Enhancement (NISE) effect. The NISE effect explains the mechanism for which some ions that normally adsorb with low affinity on external mineral surfaces will adsorb with high affinity when adsorbing onto a surface in a confining environment, the inner-sphere adsorption mechanism. Zeolite nanopore channels are well equipped to demonstrate this phenomenon.<sup>35,39,40</sup> To understand adsorption envelopes, you must look for the adsorption edges presented by the data from the experiments. The adsorption edge forms when there is a drastic change in the concentration of adsorbed ions over a very small pH range. When the data are graphed there is a drastically sharp vertical drop in the in concentration of the adsorbing ion (y-axis) as the proton concentration increases (pH decreases x-axis). The adsorption edge represents a pH threshold where protons (H<sup>+</sup>) become increasingly competitive for adsorption onto the crystal surface. This promotes an ion exchange reaction when H<sup>+</sup> adsorbs and the ion being studied (Cs<sup>+</sup> in this case) desorbs from the mineral surface. One may interpret the data from

an adsorption envelope study by positing the lower the pH of the adsorption edge the stronger the ion's affinity for adsorption is at that adsorption site, because at that site a higher concentration of protons is required to displace the ion and have it remain in solution. Typically, a pH where all the ions were able to be displaced by a very high concentration of  $H^+$  can be reached. This pH would denote the total exchange of an ion due to an overwhelming concentration of protons.

Therefore, adsorption envelope studies can help elucidate the mechanism by which  $Cs^+$  released from the FDNPP became non-exchangeable in the soil around this region of Japan and discover whether it is truly non-exchangeable. When testing the adsorption envelope of  $Cs^+$  on pure phase vermiculite, Ferreira et al. created an environment with a pH as low as 1.01 but failed to develop a final adsorption edge that lowered the amount of adsorbed  $Cs^+$  to zero (Figure 2.1).<sup>41</sup>

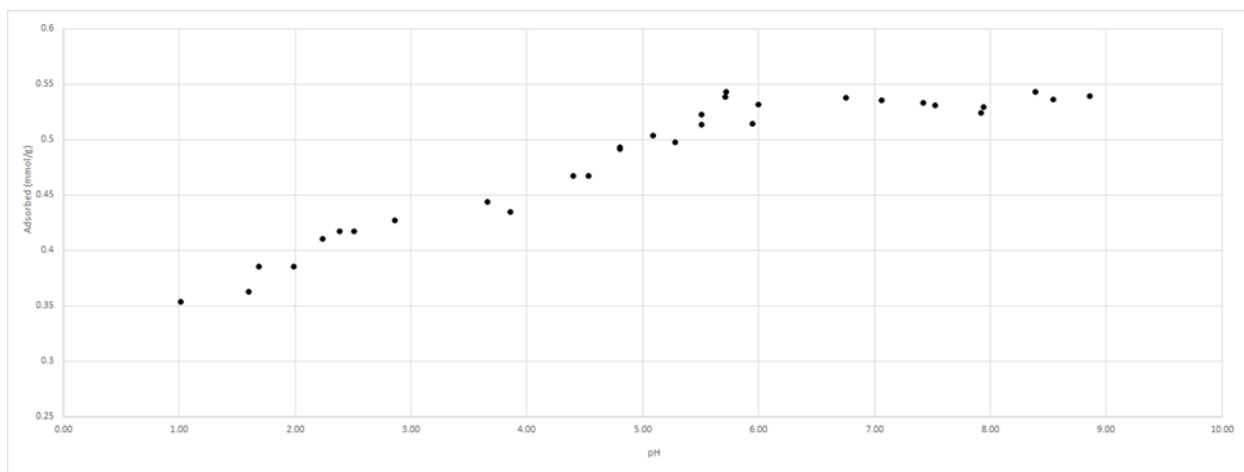


**Figure 2.1** Adsorption envelope for  $Cs^+$  on vermiculite. Two adsorption edges are present, one centered around pH 2.5 and another centered around pH 5.<sup>41</sup>

This low pH only decreased the amount of adsorbed  $Cs^+$  by 35% from the maximum adsorption capacity of  $Cs^+$  on vermiculite, which occurred at pH 8.39. To quantify this phenomenon, the concentration of  $H^+$  in the reaction vessel was increased by 7 orders of magnitude (or ten million times) but only caused a 35% reduction in the amount of  $Cs^+$  adsorbed.

Further research into the adsorption of  $\text{Cs}^+$  onto vermiculite showed that the interlayer of the clay collapses to a dimension of 0.12nm.<sup>41</sup> This size is small enough for the NISE effect to take place and cause the ion to adsorb with a strong inner-sphere mechanism. Therefore, a study was designed that would compare the adsorption of  $\text{Cs}^+$  on zeolites that are well known to strongly adsorb monovalent cations to see if this phenomenon could be replicated or if it was unique to  $\text{Cs}^+$  adsorption on vermiculite. This study compared the adsorption of  $\text{Cs}^+$  on three different zeolite minerals and compared the adsorption of  $\text{Na}^+$  and  $\text{K}^+$  on the same zeolites. This gave a comparison to the relative strength of  $\text{Cs}^+$  adsorption on zeolite nanopores of different sizes and the strength of  $\text{Cs}^+$  adsorption on these minerals with other monovalent ions. It also allowed 3 comparisons between  $\text{Cs}^+$  adsorption on the zeolites and the non-exchangeable adsorption in the 2:1 vermiculite clay.

## 2.2 *Materials and Methods*

The zeolites minerals used in these experiments were purchased from Zeolyst International in Conshohocken, PA. The Zeolites used were, ZSM-5, Zeolite Y, and Ferrierite. ZSM-5 was purchased in hydrogen-form, which means all the mineral surfaces had  $\text{H}^+$  adsorbed. Zeolite Y and ferrierite were ammonium-forms and had to be converted to  $\text{H}^+$ -forms. This was accomplished by placing the zeolites into a muffle furnace for more than 18 hours. This caused the adsorbed ammonium to volatilize as  $\text{NH}_3$  gas, leaving behind only  $\text{H}^+$ . This is a well-known method to convert ammonium-form zeolites to H-form.<sup>35</sup>

The 50-mL nominal Oak Ridge centrifuge tubes were chosen as the reaction vessel for the adsorption envelope experiments. These work well on a hematology mixer and can be used with a high-speed centrifuge. To begin the experiment approximately 0.5000g (+ 0.0030 g) of zeolite solid (ZSM-5, Zeolite Y, Ferrierite) was added to the Oak Ridge centrifuge tube. Then 7.000 mL

of 0.1 M CsOH was added to the vessel. This brings the pH of the solution to its highest value while ensuring that all samples receive the same starting concentration of Cs<sup>+</sup>. The pH was then modulated by adding varying amounts of 1.21 M HCl to the solution to reach lower pH values. The volume was equalized by adding deionized H<sub>2</sub>O until the volume of the solution equaled 35 mL in total. These samples were allowed to mix on the hematology mixer for more than 18 hours to ensure that the reaction would reach equilibrium. Following their time on the mixer the samples were centrifuged for 5 minutes at 5000 rpm and then 10 minutes at 10,000 rpm to separate the solid and liquid phases. This lets the samples experience a force of more than 7,800 g for 10 minutes. Two aliquots of the supernatant from these experiments were separated and set aside: one for pH measurements, and the other to measure the concentration of Cs<sup>+</sup>.

Inductively Coupled Plasma – Optical Emission Spectrum (ICP-OES) was used to determine the [Cs<sup>+</sup>] in solution. The instrument used was a Perkin Elmer Avio 200 and the wavelength used to measure Cs<sup>+</sup> was 894.353 nm. Both axial and radial views were used to measure the intensity for Cs<sup>+</sup> in case some concentrations were too high and would saturate the axial view. Which is much more sensitive. The data used from these experiments came from the axial view. Quality control (QC) measures were put into place to ensure the accuracy of the data and tested that the calibration was still accurate for every ten samples. If the value of the QC sample were more than  $\pm 5\%$  of the actual value the analysis would pause to allow for re-calibration. The analysis was also set up to give the average of 5 replicate readings of the intensity value for each sample.

For every experimental set, a blank was created. The blank consisted of the same amount of CsOH (7 mL) and a small amount of HCl and DI H<sub>2</sub>O to bring the solution up to the same volume as the samples. No zeolite was added to the blank, which allowed the researcher to quantify the total amount of Cs added to each sample. The initial [Cs<sup>+</sup>] ([Cs<sup>+</sup>]<sub>initial</sub>) value was gathered to calculate

the results of the experiment from the blank. The final  $[Cs^+]$  ( $[Cs^+]_{final}$ ) measured from supernatant solution after treatment and centrifugation. This allowed the amount of  $Cs^+$  adsorbed ( $[Cs^+]_{ads}$ ) to be calculated with a simple equation:  $[Cs^+]_{ads}=[Cs^+]_{initial}-[Cs^+]_{final}$ .

The best way to visualize the data from adsorption envelopes was by plotting the concentration of the analyte (adsorbed  $Cs^+$ ) as a function of the pH (X axis = pH, Y axis =  $[Cs^+]_{ads}$ ). Adsorption envelope models were used to calculate the adsorption capacity for each adsorption site.<sup>42</sup> The adsorption envelope models were created using the IExFit software Version 3.3, Distributed by alfisol.com.

**Table 2.1** Parameters for models of  $Cs^+$  adsorption on the minerals Zeolite Y, ZSM-5, and Ferrierite. From: *A Comparison of Cesium Adsorption on Zeolite Minerals to Vermiculite Clay*, D.R. Ferreira, G.D. Phillips, B. Baruah. Submitted for publication 2021. Model parameters and goodness of fit are given in Table 1. Goodness of Fit was calculated using Efreon’s pseudo  $R^2$  value using the equation  $R^2 = 1 - [\sum_i(y_i-\pi_i)^2]/[\sum_i(y_i-\bar{y})^2]$ ,  $\pi_i$  are the model’s predicted values.

Zeolite Name	Site 1		Site 2		Site 3		Pseudo $R^2$
	$\Gamma_{max}$ ( $\mu\text{mol}/\text{m}^2$ )	pK	$\Gamma_{max}$ ( $\mu\text{mol}/\text{m}^2$ )	pK	$\Gamma_{max}$ ( $\mu\text{mol}/\text{m}^2$ )	pK	
Zeolite Y	0.3240	2.0	0.5319	3.2	0.8298	5.2	0.9974
ZSM-5	2.316	2.0	1.099	6.7			0.9807
Ferrierite	2.700	1.4	1.220	6.5			0.9506

### 2.3 Results and Discussion

When examining previous research regarding other monovalent cations ( $\text{Na}^+$  and  $\text{K}^+$ ) adsorption envelopes it was noted that both  $\text{Na}^+$  and  $\text{K}^+$  adsorbed weakly on Zeolite Y and strongly on ZSM-5 and Ferrierite.<sup>35</sup> NMR analysis confirmed that  $\text{Na}^+$  was adsorbing with an outer-sphere mechanism on Zeolite Y and with an inner sphere mechanism on ZSM-5.<sup>39</sup> These results were again confirmed by a calorimetry study that looked at the heat of adsorption of monovalent ions on Zeolite Y and ZSM-5.<sup>40</sup> The size of the nanopore channels on these different zeolites was the factor that was attributed to the difference in the strength of adsorption, Zeolite Y has nanopore channels with larger dimensions than the nanopore channels of Zsm-5 and Ferrierite (table-2).

**Table 2.2** Properties of Zeolite Minerals. Pore dimensions are taken from the database of zeolite structures (<http://www.iza-structure.org/>). Surface areas provided by Zeolyst International (Conshohocken, PA).

Zeolite Name	Pore Dimensions (nm)		Pore size class	Surface Area ( $\text{m}^2 \text{g}^{-1}$ )
Zeolite Y	0.74 x 0.74	N/A	Largest	700
ZSM-5	0.51 x 0.55	0.53 x 0.56	Medium	425
Ferrierite	0.54 x 0.42	0.48 x 0.35	Smallest	400

At the beginning of this experimentation, it was assumed that a similar trend (strongly adsorbing to Ferrierite and ZSM-5, while weakly adsorbing to Zeolite Y) would be observed when  $\text{Cs}^+$  was exposed to these zeolites under the same adsorption envelope experimental method. It has also been noted that the strength of adsorption increases as the size of an atom increases. In previous studies it has been demonstrated that  $\text{Na}^+$  adsorption decreased in the presence of  $\text{K}^+$  on all three

zeolites. Potassium ( $K^+$ ) adsorbs with a higher affinity when in competition with  $Na^+$  because of this larger ionic diameter (Table 3). When considering this competitive advantage of  $K^+$  and ionic diameter in relation to zeolite nanopore channels, it is understood that  $K^+$  essentially fits more snugly into the gap; this causes adsorption to take place closer to the mineral surface and allowed for stronger electrostatic interactions between the ion and the adsorption sites. The final two factors that affect the strength of adsorption of an ion are hydration energy and hydrated diameter (Table3). Potassium ( $K^+$ ) has lower hydration energy than  $Na^+$ , meaning it can dehydrate more easily in confining environments;  $K^+$  also has a smaller hydrated diameter than  $Na^+$ , which has a similar effect.  $Cs^+$  has a larger diameter than  $K^+$ , a smaller hydrated diameter, and smaller hydration energy, (Table 3). These facts explain why  $Cs^+$  is expected to adsorb more strongly in confining environments than  $K^+$  or  $Na^+$ .

**Table 2.3** Characteristics of monovalent ions compared in this study. Ionic diameters are from Schulthess and enthalpy of hydration values were compiled by D.W. Smith.<sup>43,44</sup> A range of enthalpy of hydration values is presented to account for different methodologies for determining these values.

	Ionic Diameter (nm)	Hydrated Diameter (nm)	Enthalpy of Hydration ( $kJ\ mol^{-1}$ )
$Na^+$	0.248	0.730	390-410
$K^+$	0.318	0.696	320-330
$Cs^+$	0.392	0.692	264-280

To further explore the expected trend of  $Cs^+$  adsorbing more strongly than  $K^+$ , a recent study looked at  $K^+$  as a competitor for  $Cs^+$  in adsorption on 2:1 clay. This study used Vermiculite as the



2:1 clay, and it showed that  $K^+$  was a very ineffective competitor for ion exchange and had almost no effect on the adsorption of  $Cs^+$  in the interlayers of the clay.<sup>41</sup> This illustrated well that  $Cs^+$  adsorption in a confined environment should have a higher affinity than  $Na^+$  or  $K^+$ . The data from the adsorption envelope studies conducted on Zeolite Y, ZSM-5, and Ferrierite were able to confirm the hypothesis that  $Cs^+$  in confined environments should adsorb more vigorously than  $Na^+$  or  $K^+$  (Figure 2.2, Figure 2.3, Figure 2.4).

### $Cs^+$ adsorption envelope on Zeolite Y

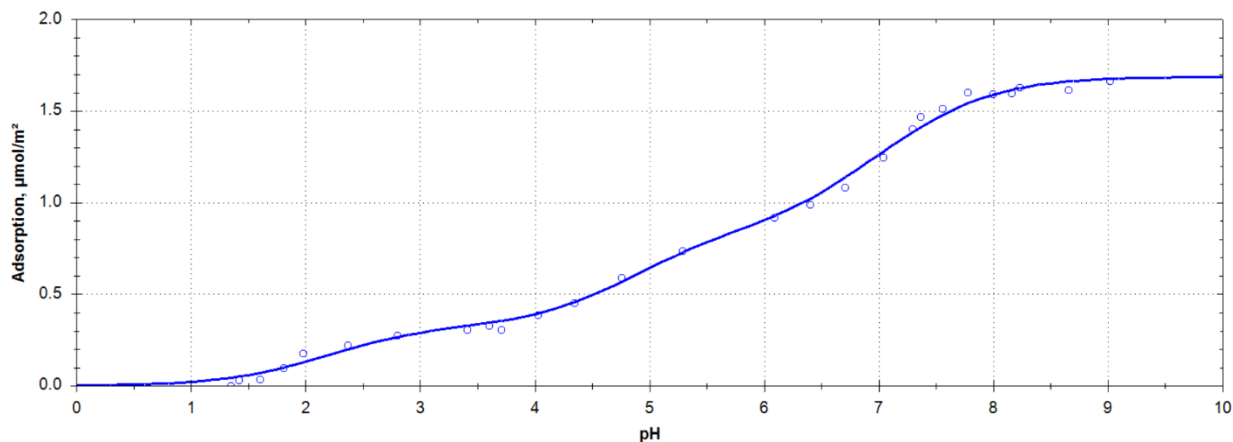


**Figure 2.2** An adsorption envelope for  $Cs^+$  on zeolite mineral Zeolite Y. The primary adsorption edge is centered at  $\sim\text{pH } 2.5$ , but has a gentle slope and a low adsorption capacity. There is a second adsorption edge centered at  $\sim\text{pH } 5$ , followed by a very slight inflection at  $\sim\text{pH } 5.8$ , followed by a third adsorption edge centered at  $\sim\text{pH } 7$ .

### Cs<sup>+</sup> Adsorption Envelope on ZSM-5

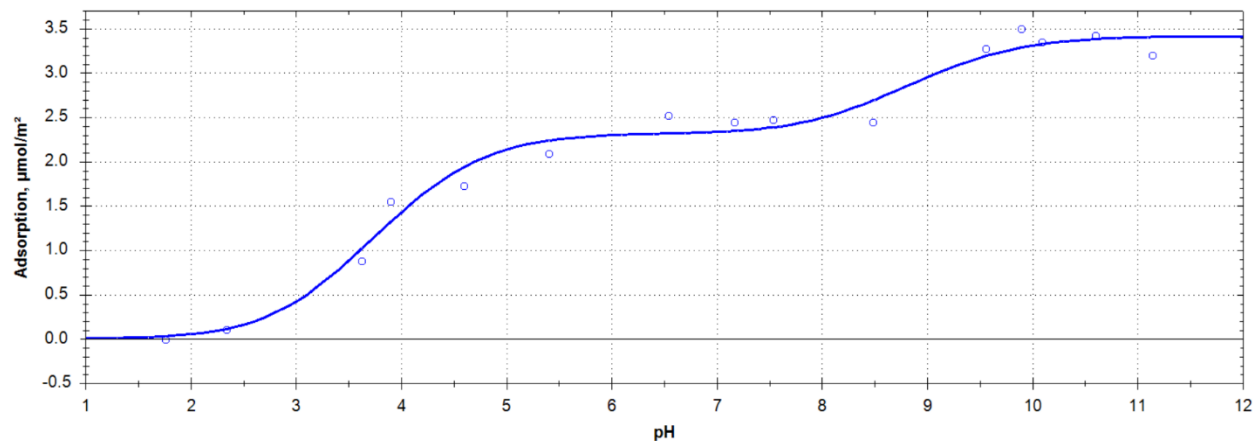


**Figure 2.3** An adsorption envelope for Cs<sup>+</sup> on zeolite mineral ZSM-5. The primary adsorption edge is steep and centered at ~pH 3.5, showing a strong adsorption mechanism for Cs<sup>+</sup> on that surface, which is presumed to be the internal sites inside the zeolite nanopores. A second adsorption edge is present, centered at ~pH 8.5 and may represent adsorption of Cs<sup>+</sup> at the intersection of the nanopores.

### Cs<sup>+</sup> Adsorption Envelope on Ferrierite

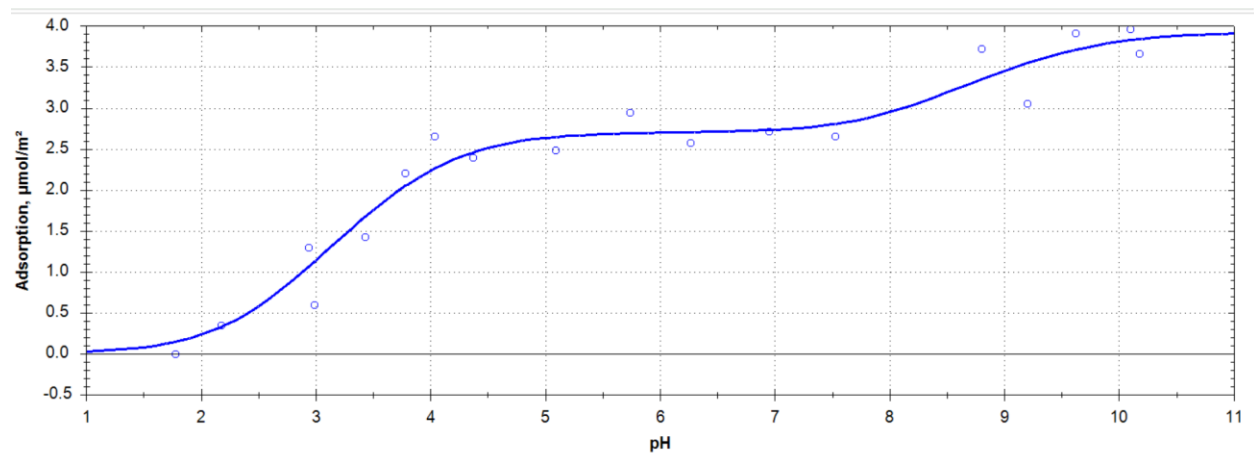


**Figure 2.4** An adsorption envelope for Cs<sup>+</sup> on zeolite mineral ferrierite. The primary adsorption edge is steep and centered at ~pH 3, showing a strong adsorption mechanism for Cs<sup>+</sup> on that surface, which is presumed to be the internal sites inside the zeolite nanopores. A second

adsorption edge is present, centered at ~pH 9 and may represent adsorption of  $\text{Cs}^+$  at the intersection of the nanopores.

When comparing  $\text{Cs}^+$  and  $\text{Na}^+$  ions the similarities stop at them both being monovalent alkali metals.  $\text{Cs}^+$  not only has a larger atomic diameter than  $\text{Na}^+$ , it also has a higher charge density than  $\text{Na}^+$ . Comparison of  $\text{Cs}^+$  adsorption to  $\text{Na}^+$  on the three zeolites tested (Fig. 5), confirms this suspicion. The  $\text{Cs}^+$  adsorption edges combine to form very similar adsorption envelopes as  $\text{Na}^+$ . However, all the adsorption edges are shifted to lower pH values indicating that  $\text{Cs}^+$  is adsorbing with a higher affinity than  $\text{Na}^+$ . This essentially means that  $\text{Cs}^+$  requires a higher  $[\text{H}^+]$  to displace it off the adsorption sites than  $\text{Na}^+$  does. Another significant difference is that the  $[\text{Cs}^+]_{\text{ads}}$  is more elevated in magnitude than  $\text{Na}^+$  when compared to the same zeolites which again displays the increased affinity for  $\text{Cs}^+$  adsorption.

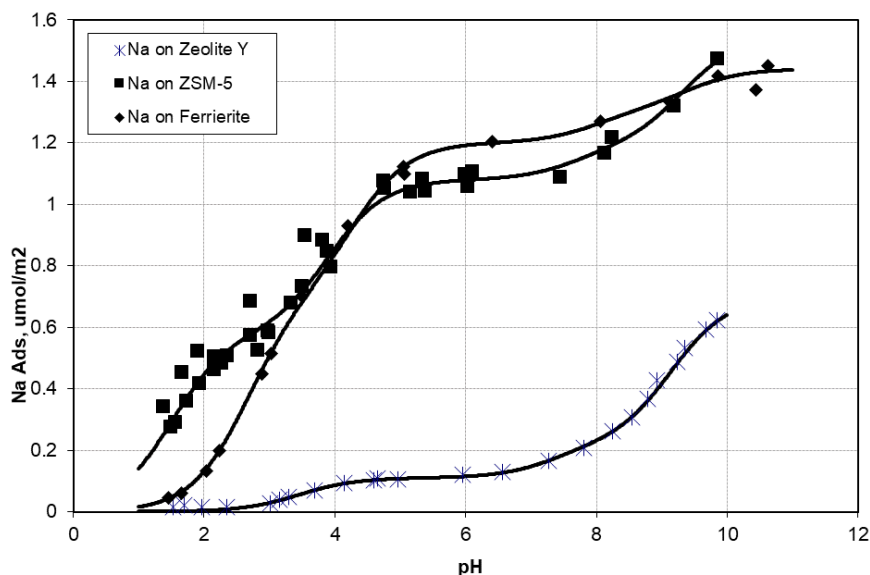


**Figure 2.5** Adsorption envelopes for  $\text{Na}^+$  on the zeolite minerals zeolite Y, ZSM-5, and ferrierite. Each envelope has two distinct adsorption edges, with  $\text{Na}^+$  showing much stronger adsorption on ZSM-5 and ferrierite than Zeolite Y. Adapted from data published in Ferreira and Schulthess, 2011.<sup>36</sup>

When visualizing the adsorption envelopes of  $\text{Cs}^+$  on the three zeolites the differences are obvious. On Zeolite Y (largest pores) the slope of the adsorption envelope is much more gradual, and the magnitude of  $\text{Cs}^+$  adsorption is much lower. Even though there are the three explicit adsorption sites represented, the data clearly showed that  $\text{Cs}^+$  adsorbs much more strongly on ZSM-5 (medium pores) and Ferrierite (smallest pores). This is a clear illustration of the expected behavior when the NISE effect takes place (Ferreira and Schulthess, 2011; Ferreira et al., 2012; Ferreira et al., 2013). Knowing that the NISE effect occurs when a cation adsorbs into an area smaller than  $\sim 0.5$  nm may help understand the nonexchangeable nature of  $\text{Cs}^+$  adsorption into vermiculite interlayers and their collapse.

Some studies have shown that ZSM-5 and Ferrierite have 3 different adsorption sites.<sup>45,46</sup> The three sites proposed within the nanopore channels on ZSM-5 and Ferrierite are the straight channel, the intersection, and the zigzag/perpendicular channel. However, data from  $\text{Cs}^+$  and  $\text{Na}^+$  adsorption envelope models showed that the two-site model had a much better fit. Suppose you make a comparison to the subtleness of the third site from Zeolite Y. In that case, it could be inferred that the resolution of these adsorption envelopes is too low, or that for the ions used in this experiment there is too little difference in adsorption on those sites. For example, it would be possible for the adsorption on the strait and zigzag channels to blend under either circumstance.

It is also important to note the similarities and differences between the adsorption envelopes of ZSM-5 and Ferrierite. They look remarkably similar; however, there are key differences driven by the smaller pore size of the nanopore channels in Ferrierite (Table 2), which explains the fact that Ferrierite has the final adsorption edge occurring at a lower pH than ZSM-5 and higher adsorption overall. The data presented from these experiments indicate there is an inverse relationship between the size of an adsorption site and the strength at which  $\text{Cs}^+$  will adsorb. XRPD analysis

showed that the diameter of the vermiculite interlayer collapses to .12 nm after  $\text{Cs}^+$  adsorption.<sup>41</sup> This is a much smaller diameter than even the smallest nanopore of ferrierite.  $\text{Cs}^+$  adsorption on vermiculite (Figure 2.1) showed just how strong  $\text{Cs}^+$  adsorption on the clay is compared to the zeolites presented in this study.

When comparing the adsorption of  $\text{Cs}^+$  on vermiculite (Figure 2.1) to the adsorption on zeolites there are two main differences to point out. The first is that the low pH adsorption edge occurs at ~pH 2.5, and the second is that the  $[\text{Cs}^+]_{\text{ads}}$  never reached zero. In fact, even lowering the pH to 1.01 only desorbed about 35% of the maximum amount of  $\text{Cs}^+$  in the solution. The difference in the behavior of  $\text{Cs}^+$  when adsorbed into the inter layer of vermiculite compared to the nanopore channels of zeolites is remarkable and helped further the understanding of just how high an affinity vermiculite has for  $\text{Cs}^+$ .

## **CHAPTER 3. COMPARING SELECTIVE PRECIPITATION AGENTS**

### **3.1 Introduction**

Many remediation techniques for the removal of  $\text{Cs}^+$  from the landscape have been proposed, including using algae as a bioremediation vector to remove  $^{137}\text{Cs}$  from water.<sup>47</sup> Zeolite adsorbents have been used to remove group one and two elements from solutions but there is then the issue of removing the zeolite from the substrate following treatment.<sup>48</sup> Temperature-responsive polymer/magnetic/zeolite composite sorbent separation was shown to work by Nakamarua et al.<sup>45</sup> However, this was a very complicated process that would be difficult to conduct in highly heterogenous conditions like on natural soil. Sato et al. reported  $^{137}\text{Cs}$  could be removed from water by a saponite clay adsorbent, which highlighted that there are many ways to remove  $\text{Cs}^+$  from aqueous solutions but a more sophisticated method of decontamination would be required for  $\text{Cs}^+$  removal from a soil substrate.<sup>49</sup>

Saito et al. developed a method that could facilitate the remediation of  $\text{Cs}^+$  from a complex substrate like soil. This study focused on the removal of  $\text{Cs}^+$  using the reagent sodium tetrakis (4-fluorophenyl) borate hydrate ( $\text{NaTFPB}$  or  $\text{TFPB}$ ) and sodium tetraphenylborate ( $\text{NaTPB}$ ) (Saito, 2021). A previous study demonstrated that  $\text{Cs}$ - $\text{TFPB}$  precipitate could be obtained with great efficiency between the pH range of 0.7 to 10.8.<sup>50</sup> A recent study demonstrated the effectiveness of treating  $\text{Cs}^+$  doped pure phase vermiculite with 20mM  $\text{TFPB}$  in a solution of 0.4 M  $\text{Mg}(\text{NO}_3)_2$ . The results of this study indicated that the  $\text{Cs}^+$  was able to be replaced by  $\text{Mg}^+$  within the interlayers of the clay after 2 hrs.<sup>1</sup> Saito et al. achieved an efficiency of 89.4% desorption, but this required a 1:10  $\text{Cs}:\text{TFPB}$  molar ratio.<sup>51</sup> However, even with a desorption efficiency of almost 90%  $\text{TFPB}$  is a prohibitively expensive reagent, making treatment with it non-cost-effective.

A cheaper alternative might be found through the use of polyoxometalates as an alternative precipitation agent to TFPB. Three polyoxometalates (POMs) have been shown to precipitate with  $\text{Cs}^+$  in solution. Polyoxometalates are highly ionic compounds made of multiple transition metals linked with oxygen and often coordinated with phosphorus, silicon, or other coordinating atoms. They have sizes in the range of 1 to 3 nm and possess unique properties.<sup>52-54</sup> One of the unique properties of POMs is that some of them can precipitate from solution exclusively with  $\text{Cs}^+$ .

There are two families of POMs: Isopoly compounds, which are composed of one type of  $d^0$  metal cations, and heteropoly compounds, which are comprised of a metal-oxide framework with a combination of p-, d-, or f-block hetero atoms.<sup>53,55</sup> Dr. James F. Keggin determined the first heteropolyoxometalates phosphotungstic acid (PTA),  $\text{H}_3\text{PW}_{12}\text{O}_{40}$ , by identifying its X-ray crystal structure.<sup>56</sup> This study focused on the use of some Keggin-type POMs, type phosphotungstic acid,  $\text{H}_3\text{PW}_{12}\text{O}_{40}$  (PTA), silicotungstic acid,  $\text{H}_4\text{SiW}_{12}\text{O}_{40}$  (STA), and molybdovanadophosphoric acid,  $\text{H}_5\text{PMo}_{10}\text{V}_2\text{O}_{40}$  (MVPA) along with TFPB as a reference. The initial hypothesis was that the POMs would precipitate after all their protons had exchanged with  $\text{Cs}^+$ . Therefore, PTA, STA, and MVPA (Figure 3.1) would precipitate from solution with 3, 4, and 5,  $\text{Cs}^+$  respectively.<sup>57,58</sup> This exchange would form an insoluble precipitate that could help remove  $\text{Cs}^+$  from a complex substrate like vermiculite (Scheme 3.1).

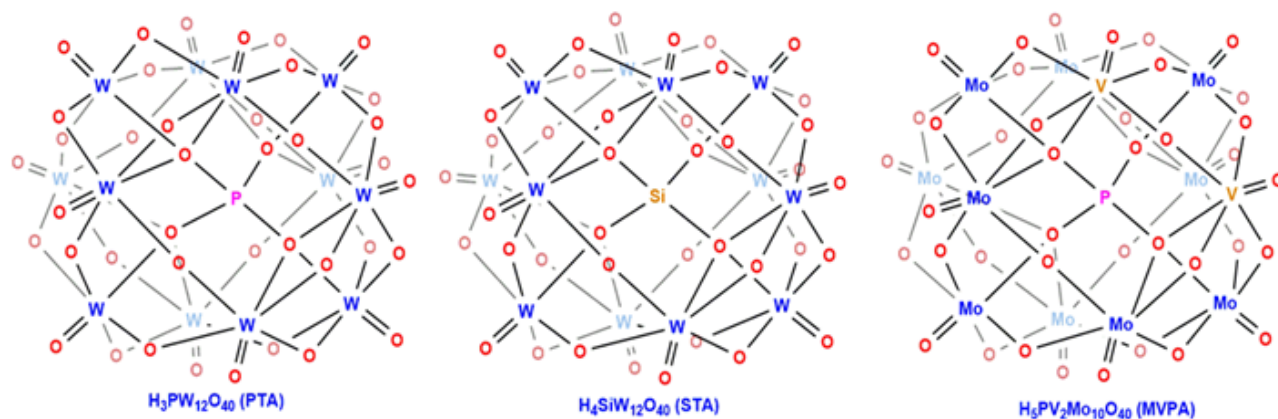
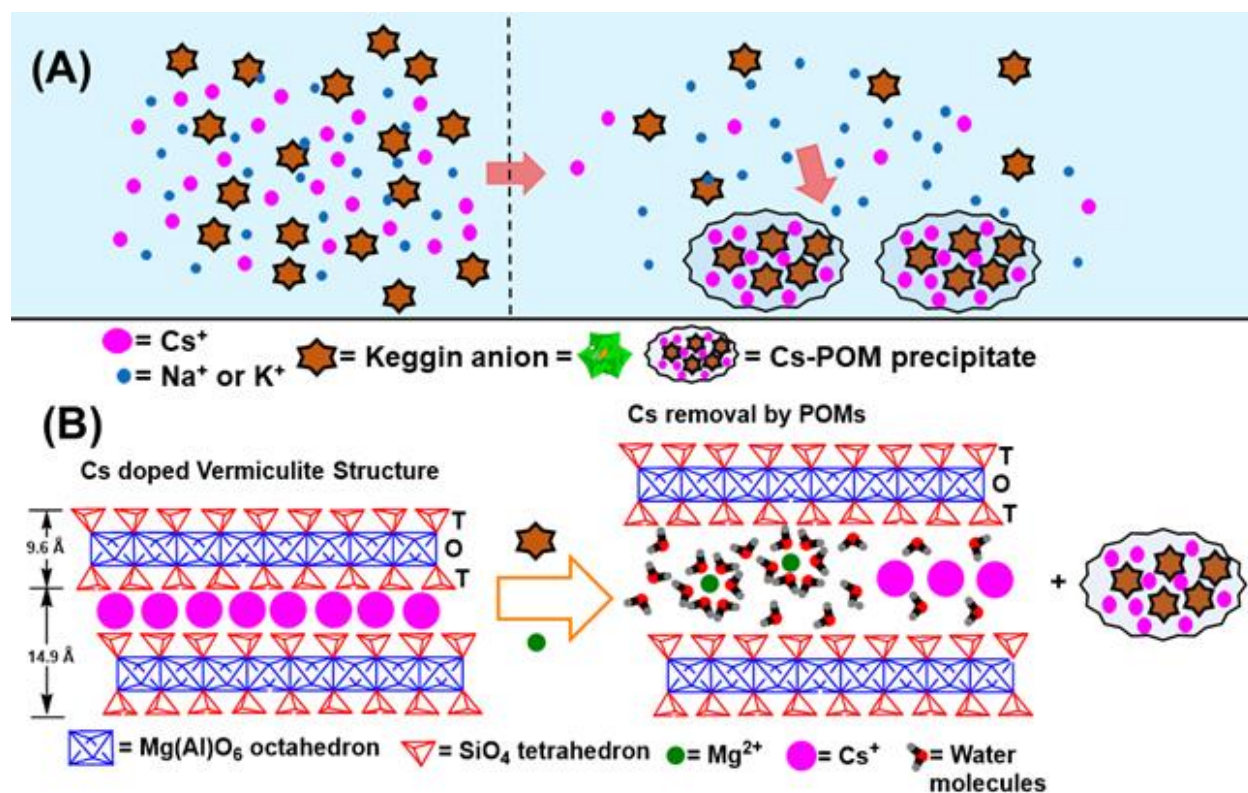


**Figure 3.1.** Molecular structures of Keggin type POMs PTA, STA, and MVPA.



**Scheme 3.1** Proposed selective precipitation formation phenomenon between Keggin type POM and Cs<sup>+</sup> (A) in the presence of Na<sup>+</sup> and K<sup>+</sup>. (B) Cs<sup>+</sup> removal by POM from Cs-doped pure phase vermiculite in the presence of Mg<sup>2+</sup>



### 3.2 Materials and Methods

For the synthesis and other trials of these experiments, Molybdovanadophosphoric acid,  $H_5PMo_{10}V_2O_{40}$  (MVPA), and silicotungstic acid,  $H_4SiW_{12}O_{40}$  (STA) were synthesized in the lab using well known methods.<sup>59,60</sup> They were all characterized with Fourier-transform infrared spectroscopy (FTIR), X-ray powder diffraction (XRPD), UV-visible spectroscopy (UV-vis) and Raman spectroscopy. Sodium tetrakis(4-fluorophenyl)borate dihydrate (TFPB) was purchased from Fisher Scientific. Phosphotungstic acid,  $H_3PW_{12}O_{40}$  (PTA) was purchased from Sigma-Aldrich. Hydrochloric acid (HCl), Cesium Hydroxide (CsOH), Cesium Chloride (CsCl), were all Certified ACS grade or higher.

### 3.3 Synthesis of $H_5PMo_{10}V_2O_{40}$ (MVPA)

16.5 g  $MoO_3$  and 1.6 g of  $NH_4VO_3$  were added to 250 mL of deionized water and heated in a round bottom flask with a reflux condenser until fully dissolved. Once the solution reached 120°C 0.789mL of concentrated phosphoric acid (85%) was added drop wise to the round bottom flask. This produces a clear red solution. The orange-red solid after solvent evaporation was recrystallized from DI as our product.<sup>59</sup>

### 3.4 Synthesis of $H_4SiW_{12}O_{40}$ (STA)

To synthesize  $2H_4SiW_{12}O_{40}$  (STA) 12-tungstasilic acid, first sodium tungstate dihydrate was heated and dissolved in water. Once dissolved the flask was removed from the heating mantle, a solution of 12.5% sodium silicate was added to the sodium tungstate dihydrate solution by micropipette. The reaction vessel was returned to the heating mantle and the solution was heated until boiling. While stirring vigorously, 7.5 mL of concentrated HCl was added to the reaction via dropping funnel over a 10-minute period, approximately 12 drops per minute. The solution was filtered, and the residue and supernatant were both saved. The supernatant held the product, which was extracted with ether in a separatory funnel. Two layers formed in the ether, the pure STA was

found in the bottom layer, crystals were grown as the ether evaporated. Once the STA crystals formed the sample was baked at 70°C to ensure all ether had evaporated from the crystals before characterization.<sup>60</sup>

### *3.5 Characterization and Spectroscopy*

The POMs were characterized using FTIR, UV-vis, Raman spectroscopy, and XRPD analysis.

### *3.6 ICP Measurements*

The supernatant from the stoichiometry and speciation trials was analyzed on ICP to look for the concentration of Cs<sup>+</sup> in the solution. The concentration of the precipitation agent was also verified by measuring the intensity of tungsten for STA and PTA, Molybdenum for MVPA, and Boron for TFPB. The calibration solutions for Cs<sup>+</sup> consisted of a blank (0 mM), 1 mM, 5 mM, 10 mM, and 15 mM solutions. For the precipitation agent analysis, the calibration solution concentrations were lowered to 0.1 mM, 0.5 mM, 1 mM, and 5 mM because the concentration of the POMs and TFPB were an order of magnitude below the [Cs<sup>+</sup>]<sub>int</sub>. Since the reaction with Cs<sup>+</sup> removes the POMs from the solution, there was also the possibility of all the POM precipitating out of the solution resulting in a very low to null concentration. When analyzing for tungsten and molybdenum there is also resolution benefit because of the molar ratios of tungsten to phosphorus/silicon in PTA/STA (12:1), and the molar ratios of molybdenum to phosphorus in MVPA (10:1)

### *3.7 Understanding Speciation of POMs & Stoichiometry of POMs and TFPB*

The speciation curves of each POM should directly correlate with its ability to precipitate Cs from the solution. To test this reaction environments were created at different pH values. Once the most effective pH values were confirmed for each POM, experiments were replicated at those pHs to determine a ratio of the average moles of Cs precipitated per mole of POM.

This experiment was performed in a 50 mL Oak Ridge centrifuge tube. The total volume of the reaction was always 35 mL. 7 mL of 0.1M Cs salt was added to the centrifuge tube. CsOH was beneficial for this experiment to reach higher pH values. Next, 21 mL of DI plus HCl was added to the centrifuge tube. This step was to adjust the pH of the solution. For example, if 1 mL of HCl was used 20 mL of DI was added to the reaction vessel to reach the total volume required. Finally, 7 mL of 0.01 M ligand (TFPB, PTA, MVPA, STA) was added. The samples were left to mix on a hematology mixer for more than 60 hours until optimal kinetics were discovered. After the samples were successfully mixed, they were centrifuged for 5 minutes at 5,000 rpm followed by 10 minutes at 10,000 rpm. This formed a pellet of solid precipitate at the bottom of the reaction vessel. The supernatant was extracted and 5 mL of it was placed into a 15 mL conical tipped centrifuge tube. This sample was prepared for ICP by diluting the solution by 50% to ensure that the optics would not be saturated on the ICP. Also 10 mL of the solution was placed into a test tube for pH measurement. The dilute supernatant was then measured on the ICP using a calibration curve comprised of a fresh DI blank, 1mM, 5mM, 10mM, and 15mM solution.

### *3.8 POM Precipitation Controls*

Controls were used to determine that the POMs would only precipitate in the presence of Cs. The reactions were set up as listed above but instead of using CsOH,  $\text{Mg}(\text{NO}_3)_2$  or KOH were used. Also, a multi-ion control was conducted in which the STA and PTA were exposed to CsCl,  $\text{Mg}(\text{NO}_3)_2$ , and KCl at equal concentrations in the solution to prove the true selectivity of the POMs for Cesium.

### *3.9 Results and Discussion*

#### *Characterization of POMs*

The Keggin type POMs were characterized using routine techniques, FTIR, Raman spectroscopy, UV-vis spectroscopy, and XRPD. Using FTIR to observe the characteristic bond stretching and

bending vibrations of the molecules is commonplace in the characterization of POMs. The POMs spectra and the spectra of the comparable POM-Cs precipitate are presented in Figure 3.2 and Table 3.1. Literature reported the characteristic FTIR adsorption sites for Keggin STA are at 976 (W=O), 922 (Si-O), 879 (W-Oc-W corner sharing) and 770  $\text{cm}^{-1}$  (W-Oe-W edge sharing).<sup>61</sup> The signals of the STA sample used in this study were 967 (W=O), 908 (Si-O), 878 (W-Oc-W corner sharing), and 754  $\text{cm}^{-1}$  (W-Oe-W edge sharing). The signals of the synthesized STA sample used in this study were 967 (W=O), 908 (Si-O), 878 (W-Oc-W corner sharing) and 754  $\text{cm}^{-1}$  (W-Oe-W edge sharing). The STA-Cs precipitate (see fig 3.2 and table 3.1) had adsorptions at 981 (W=O), 921 (Si-O), 887 (W-Oc-W corner sharing), and 781  $\text{cm}^{-1}$  (W-Oe-W edge sharing). Literature reports the characteristic FTIR absorption sites for Keggin PTA were 1080 (P-O), 985 (W=O), 890 (W-Oc-W corner sharing) and 839  $\text{cm}^{-1}$  (W-Oe-W edge sharing).<sup>62</sup> The signals for the purchased PTA utilized for this project were 1052 (P-O), 964 (W=O), 877 (W-Oc-W corner sharing) and 818  $\text{cm}^{-1}$  (W-Oe-W edge sharing), whereas the Cs bound PTA (PTA-Cs, see Table 1) absorptions were 1077 (P-O), 980 (W=O), 885 (W-Oc-W corner sharing) and 828  $\text{cm}^{-1}$  (W-Oe-W edge sharing). For Keggin MVPA the Characteristic FTIR adsorption sites were 1064 (P-O), 961 (M=O), 867 (Mo-Oc-Mo corner sharing) and 780  $\text{cm}^{-1}$  (Mo-Oe-Mo edge sharing) as reported in the literature.<sup>63</sup> The signals for the MVPA synthesized for use in this project were 1061 (P-O), 927 (M=O), 849 (Mo-Oc-Mo corner sharing) and 761  $\text{cm}^{-1}$  (Mo-Oe-Mo edge sharing) and the Cs bound MVPA (MVPA-Cs, see Table 1) were 1064 (P-O), 929 (M=O), 847 (Mo-Oc-Mo corner sharing) and 755  $\text{cm}^{-1}$  (Mo-Oe-Mo edge sharing).

Signals at 3136 and 1696  $\text{cm}^{-1}$  represented -OH stretching and the bending vibrations of H-O-H.<sup>64</sup>

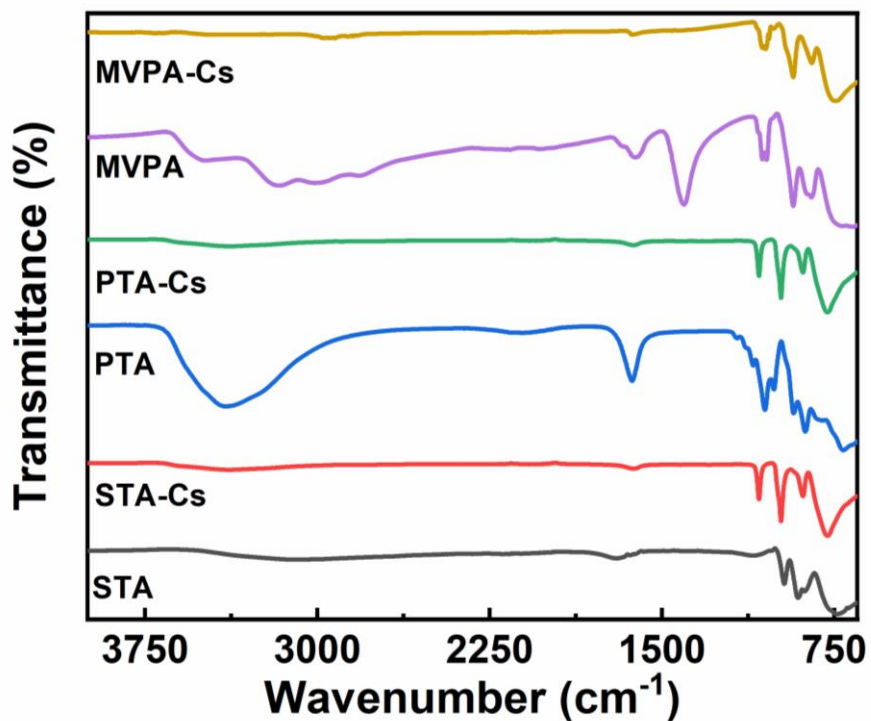


**Figure 3.2.** The FTIR spectra of STA, STA-Cs, PTA, PTA-Cs, MVPA and MVPA-Cs.

**Table 3.1.** The FTIR signal assignments of STA, STA-Cs, PTA, PTA-Cs, MVPA, and MVPA-Cs.

(cm <sup>-1</sup> )	STA	STA-Cs	PTA	PTA-Cs	MVPA	MVPA-Cs
$\nu_{\text{Si-O}}$	908	921	-	-	-	-
$\nu_{\text{P-O}}$	-	-	1052	1077	1061	1064
$\nu_{\text{W=O}}$	967	981	964	980	-	-
$\nu_{\text{M=O}}$	-	-	-	-	927	929
$\nu_{\text{V=O}}$	-	-	-	-	-	-
$\nu_{\text{O-Wc-O}}$	878	887	877	885	-	-
$\nu_{\text{O-We-O}}$	754	781	818	828	-	-
$\nu_{\text{O-Moc-O}}$	-	-	-	-	849	847
$\nu_{\text{O-Moc-O}}$	-	-	-	-	761	755

All three POMs were characterized by Raman spectroscopy Figure 3.3. The  $W=O_t$  symmetric stretching and  $W=O_t$  asymmetric stretching of STA are seen at 1001 and 972  $cm^{-1}$  respectively.<sup>65</sup> The W-O-W stretching Raman bands of STA are seen at 892  $cm^{-1}$ .<sup>65</sup> The signals at 557 and 244  $cm^{-1}$  were related to the O-Si-O bending and the W-O (silicon linked) bending of Keggin STA.<sup>65</sup> The structure of PTA shared many similarities to STA; the  $W=O_t$  symmetric stretch, the  $W=O_t$  asymmetric stretch, and the W-O-W stretching signals are at 1012  $cm^{-1}$ , 1002  $cm^{-1}$ , and 911  $cm^{-1}$  respectively.<sup>66</sup> The additional signal at 548  $cm^{-1}$  is related to O-P-O stretching, and the signals at 244, 221, and 208  $cm^{-1}$  are related to bending in the phosphate ( $PO_4^{3-}$ ) unit.<sup>67</sup> The MVPA structure was different from the two previous Keggin compounds; MVPA had Raman signals for  $Mo-O_t$  symmetric stretching,  $Mo-O_t$  asymmetric stretching, and Mo-O-Mo at 980, 953, and 875  $cm^{-1}$ , respectively. Signals for O-P-O stretch and  $PO_4^{3-}$  unit bending were 611, 264 and 223  $cm^{-1}$ , respectively.<sup>68,69</sup>

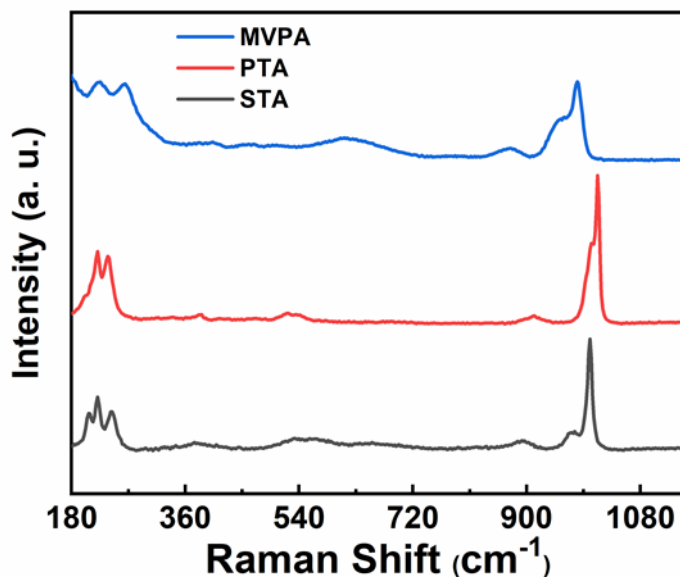


**Figure 3.4** The Raman spectra of STA, PTA, and MVPA.

The UV-vis Spectra of STA, PTA and MVPA are shown in Figure 3.4. Literature reported an absorption band characteristic attributed to  $W(d) \rightarrow O(2p)$  charge transfer at 264 nm.<sup>70</sup> For STA in aqueous solution there was a strong absorption band at 263 nm and for PTA there was a strong band at 260 nm, these were both attributed to the  $W(d) \rightarrow O(2p)$  charge transfer and corresponded with findings from literature.<sup>71-73</sup> When examining the UV-vis spectra of MVPA, there was an absorption band at 236 nm. The band is attributed to the  $Mo(d) \rightarrow O(2p)$  charge transfer.<sup>68</sup> The results of this UV-vis study confirm that STA, PTA, and MVPA remain intact in an aqueous solution.

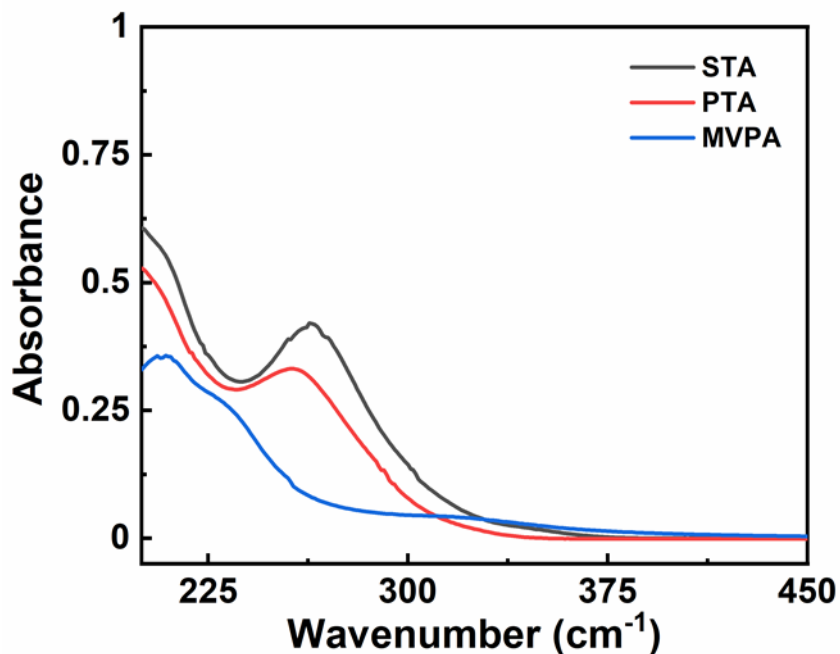


**Figure 3.5** The UV visible spectra of STA, PTA, and MVPA.

The XRPD patterns of the STA, PTA and MVPA used in this experiment are presented in Figure 3.5. Four Peaks associated with the body-centered cubic secondary structure of the Keggin anion were found at 8.8, 10.6, 25.7, and 34.9  $2\theta$  values. These values were representative of the values found in the literature.<sup>65</sup> Similarly for PTA peaks at 8.2, 11.2, 28.4, 32.6, 46.7, and 58.6 suggests

a good crystal structure for PTA.<sup>66</sup> The MVPA XRPD spectrum depicted the XRPD peaks reported in the literature for the compound.<sup>74,75</sup>

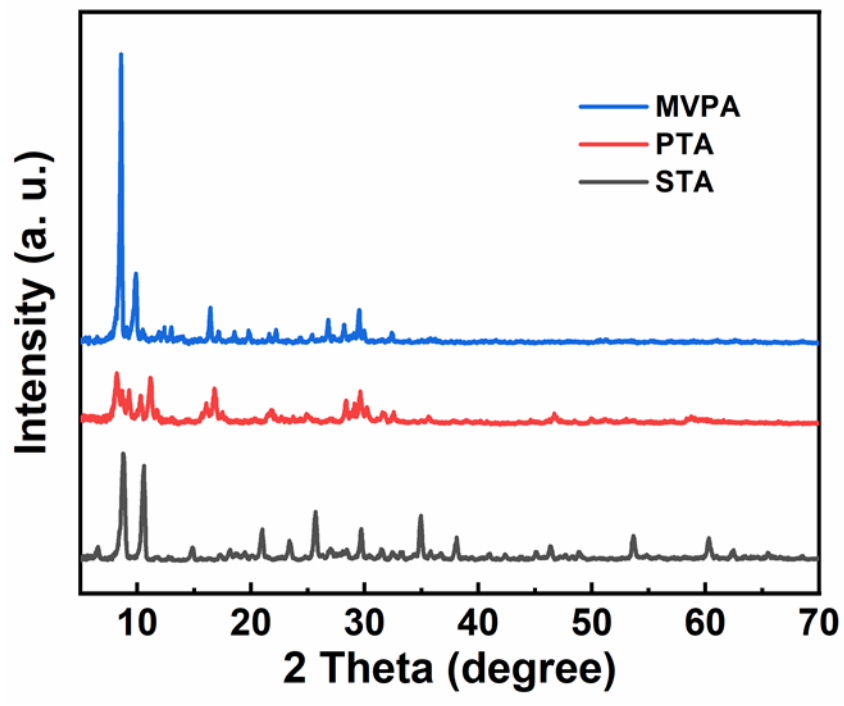


**Figure 3.6** The XRPD plots of STA, PTA, and MVPA.

#### *Speciation Compared to Extraction Potential and Precipitation study by Precipitants*

To better understand the selective precipitation agent's ability to remove  $\text{Cs}^+$  from solution, a better understanding of the POMs speciation and their ability to extract  $\text{Cs}^+$  at different pH values was evaluated. Many POMs exist only in specific pH ranges while in solution. For example, PTA is only highly present below pH 2.4.<sup>76</sup> MVPA is only highly stable below pH 5.6.<sup>77</sup> Little data was found about the speciation of STA and although TFPB would not have a speciation concern, its ability to act as an acid should certainly be hindered at some pH. When testing STA across a pH range using the method that was used for the other samples no pH above 2.95 was able to be reached. This indicated that it was able to sufficiently acidify the solution without the help of any additional HCl. The results for MVPA (Figure 3.7) indicated that for best extraction potential, the



solution needs to be below pH 6, which is supported by the literature. Likewise for the PTA trial (Figure 3.8) the results indicated that the most efficient extraction with this POM took place below pH 2.0. When the trials for TFPB (Figure 3.9) began, it was assumed that it would probably not function well at low pH. This was confirmed and the pH of extractions using TFPB would need to be above 4.0. These results determined that the POMs would be acidified with HCl when testing their stoichiometry and testing extractions on a soil substrate, but TFPB would not need any acid included in the treatment solution.

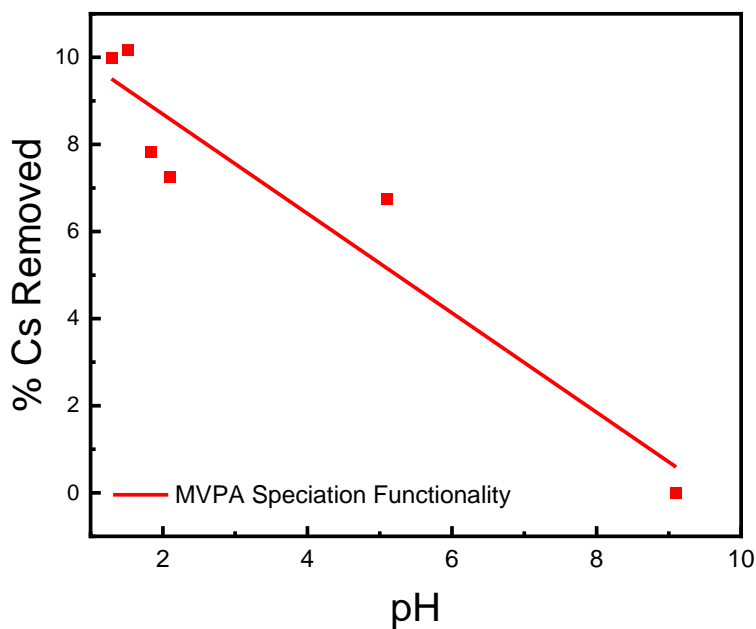


**Figure 3.7** Visualization of the speciation of MVPA by analyzing the extraction potential of Cs<sup>+</sup> removal across a pH range.

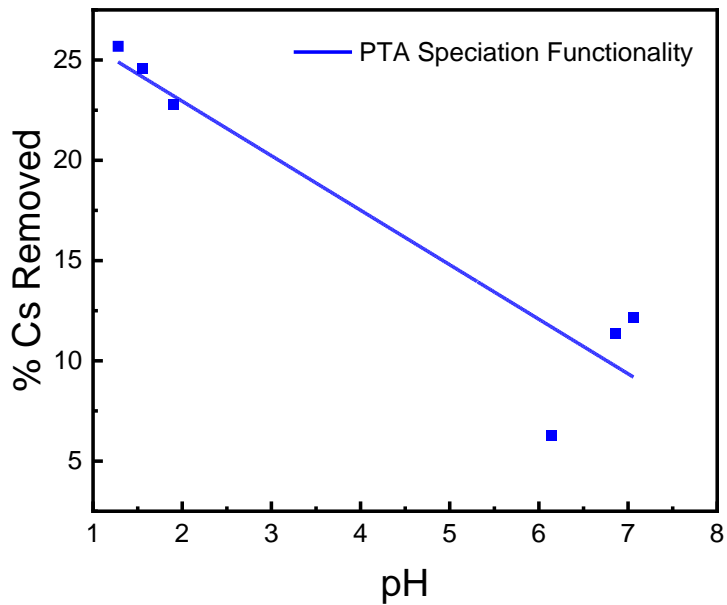


**Figure 3.8** Visualization of the speciation of PTA by analyzing the extraction potential of Cs<sup>+</sup> removal across a pH range.

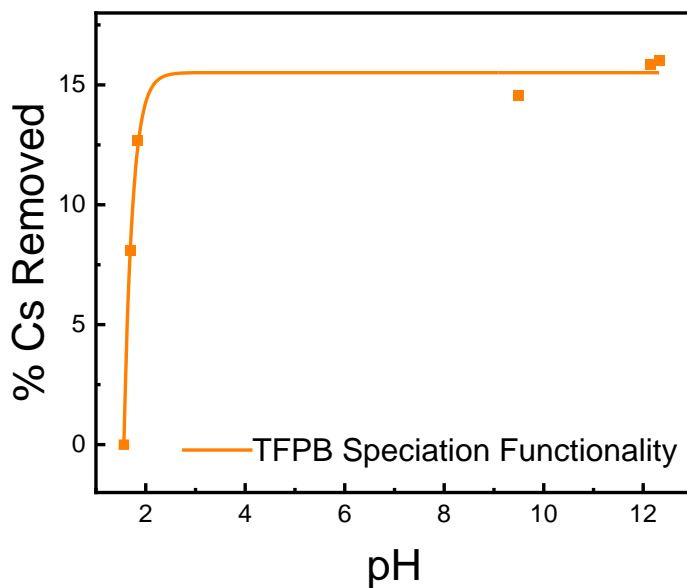


**Figure 3.9** Comparing the extraction potential of TFPB to POMs over a similar pH range. Note the drastic change in TFPB efficacy over a small pH change at the lower end of the scale and the inverse relationship the ligand has with protons compared to POMs.

In Table 3.2 the results for the stoichiometry trials of the ionic precipitation agents are listed. These samples were exposed in an aqueous solution to a known amount of  $\text{Cs}^+$  and the appropriate pH to maximize the effectiveness of their speciation. The samples were then exposed to the centrifugal force of 7,800g for ten minutes. This caused any precipitate to form a pellet at the bottom of the tube and allowing the supernatant to be extracted for analysis on the ICP-OES. The supernatant was analyzed for  $\text{Cs}^+$ , and the pH was recorded to ensure the sample fell within the optimal pH range for each precipitation agent. The samples were also allowed to mix for more than 60 hours to ensure equilibrium was met. The calibration curve used to analyze these samples consisted of a DI blank (0 mM), 0.1 mM, 0.5 mM, 1.0 mM, and 5.0 mM. To analyze for the selective precipitation agents, W and Mo were used for the POMs and B was used for TFPB. The benefit of using W and Mo when analyzing for the POMs was an increased resolution because of the molar ratios of these elements within the compounds (12:1 W:PTA/STA and 10:1 Mo:MVPA). From the data presented in Table 3.2 it is apparent that STA greatly outperformed the other compounds in both efficiency and efficacy. STA was able to remove 4.13  $\text{Cs}^+$  per molecule and was able to remove 39.82% of the  $\text{Cs}^+$  from the treatment solution. PTA followed closely behind removing 2.32  $\text{Cs}^+$  per PTA molecule and removing 26.42% of the  $\text{Cs}^+$  from the solution. MVPA and TFPB were closely tied in terms of efficiency; however, the concentration of MVPA in solution upon analysis was about half that of the other precipitation agents resulting in its %  $\text{Cs}^+$  removed value being about half the TFPB value. MVPA and TFPB removed 1.17 and 1.16  $\text{Cs}^+$  per molecule respectively, while they extracted 7.72% and 15.47% of the  $\text{Cs}^+$  from solution respectively. When looking at the structures of MVPA ( $\text{H}_3\text{PMo}_{10}\text{V}_2\text{O}_{40}$ ), STA ( $\text{H}_4\text{SiW}_{12}\text{O}_{40}$ ), and PTA ( $\text{H}_3\text{PW}_{12}\text{O}_{40}$ ) it was hypothesized that the number of total replaceable protons would dictate the POMs extraction potential. That would mean that MVPA would be able to extract 5  $\text{Cs}^+$  per molecule, STA 4, and PTA 3. However, after

reviewing the current literature, this was found not to be the case. PTA is known to replace 2.5 H<sup>+</sup> by forming Cs<sub>2.5</sub>H<sub>0.5</sub>PW<sub>12</sub>O<sub>40</sub>.<sup>78</sup> STA is known to bind up to 4 Cs<sup>+</sup>.<sup>65,79</sup> MVPA is known to bind 2.5-3.5 Cs<sup>+</sup>.<sup>80</sup> The data from table 3.2 for STA and PTA were consistent with findings in the literature, but MVPA presented a much lower value. TFPB is an ion with a charge of -1. The study that initially investigated the forced desorption of Cs<sup>+</sup> from vermiculite by Tamura et al. demonstrated the ligands 1:1 Cs<sup>+</sup>:TFPB desorption ratio further supported by the data presented in the table 3.2.<sup>1</sup>

TABLE 3.2 Stoichiometry Results

Precipitation Agent	Optimal pH	mmoles Cs Removed	% Cs Removed	Cs Removed Per molecule
TFPB	Above 7	0.0812	15.47%	1.16±0.06
MVPA*	Below 4	0.0484	7.72%*	1.17±0.12
PTA	Below 2	0.166	26.42%	2.32±0.17
STA	Below 3**	0.245	39.82%	4.13±0.16

\*MVPA concentration in the blank was ½ of the other precipitation agents

\*\*STA speciation trials pH failed to rise above 2.95

### *Control Results*

No precipitation was observed when exposing POMs to ions other than Cs<sup>+</sup> including Mg(NO<sub>3</sub>)<sub>2</sub> and KOH. The supernatant of these solutions was analyzed via ICP-OES these results confirmed that no precipitation had taken place compared to the blank solutions prepared for each analyte.

The results from a similar control experiment indicated the POMs selectivity for precipitating with Cs. A precipitate formed almost immediately when exposing PTA and STA to a solution of CsCl and Mg(NO<sub>3</sub>)<sub>2</sub>. The supernatant from these solutions was analyzed for Mg<sup>2+</sup> and Cs<sup>+</sup>. The supernatant had much less Cs<sup>+</sup> than the stock solutions and slightly less Mg(NO<sub>3</sub>)<sub>2</sub>. This was

expected because of the length of time the solution had been allowed to mix. Some adsorption onto the surface of the precipitate itself may have taken place. A further simple experiment was conducted where this precipitate was gently washed and placed in a dilute solution of  $\text{Ca}^{2+}$  to test the exchange of some  $\text{Cs}^+$  and  $\text{Mg}^{2+}$  from the metal oxide outer rings of the Keggin-type POM precipitate surfaces. The supernatant of this simple ion exchange experiment was analyzed, and the results concluded that the  $\text{Mg}^{2+}$  from the control experiment had adsorbed onto the surfaces of the precipitate and was able to be displaced by  $\text{Ca}^{2+}$ .

## **CHAPTER 4. FORCED PRECIPITATION OF NON-EXCHANGABLE Cs IN PURE PHASE VERMICULITE**

### *4.1 Introduction*

When designing a remediation strategy for the soil surrounding the FDNPP two major discoveries affected the methods used to decontaminate the landscape of the exclusion zones. First, the discovery that the radioactive  $^{137}\text{Cs}$  and  $^{134}\text{Cs}$  (radiocesium) was primarily sequestered in the top layers of the soil justified the removal and storage of the topsoil from the area.<sup>81,82</sup> Second, the discovery that the adsorption of  $\text{Cs}^+$  into the interlayers of the 2:1 clay in the region resulted in the ion being non-exchangeable (short of fully digesting the mineral) meant that normal soil remediation methods would not be useful when trying to decontaminate the soil from the region.<sup>83-</sup>

<sup>91</sup> Normal soil remediation methods, such as displacing the radionuclide with  $\text{Ca}^{+2}$  or  $\text{NH}_4^+$  and flushing the  $\text{Cs}^+$  into the groundwater, would have little to no effect at removing  $\text{Cs}^+$  from the clay. Therefore, the soil had to be removed and no immediate treatment was attempted. This left the Japanese government with more than 15 million  $\text{m}^3$  of soil and no long-term storage plan. To visualize the size of this problem the volume of the Mercedes Benz Super Dome is 3.5 million  $\text{m}^3$ . Essentially if the clay were extracted from the soil the total volume of radioactive material that would need to be stored could be reduced, and if there was a way to force the extraction of radiocesium from the clay the total volume of radioactive waste could be significantly reduced. This led Tamura et al. to develop a method that would force the desorption of non-exchangeable  $\text{Cs}^+$  from doped pure phase vermiculite (doped vermiculite has been exposed to high concentrations of  $\text{Cs}^+$  solution until the interlayers collapse and the Cation Exchange Complex (CEC) is dominated by  $\text{Cs}^+$ .<sup>1</sup> The CEC is the mechanism where ions exchange between the adsorbed form (ads) and the aqueous state (aq). When an ion becomes non-exchangeable, it

dominates the CEC equilibrium until almost all the adsorbed ions are of one type. The method proposed by Dr. Tamura treated the pure phase clay with a solution of  $\text{Mg}(\text{NO}_3)_2$  and a ligand, sodium tetrakis (4-fluorophenyl) borate (TFPB). TFPB has the property of precipitating when bound with  $\text{Cs}^+$  but does not precipitate with  $\text{Mg}^{2+}$ . When the doped vermiculite was placed in this solution a white precipitate began to form. This was effectively able to remove Cs from the equilibria and force the desorption thereafter. XRPD data also demonstrated that after this treatment the interlayers of the vermiculite had increased in diameter meaning that the  $\text{Cs}^+$  precipitating with the TFPB was indeed from the interlayers of the clay.<sup>1</sup> This method worked because the non-exchangeable nature of the  $\text{Cs}^+$  in the vermiculite exists in an equilibrium that just lies extremely far to the side of  $\text{Cs}^+_{\text{ads}}$ . The  $\text{Mg}^{2+}$  could, when in a concentrated solution, force a small amount of  $\text{Cs}^+$  out of the interlayer of the clay, but on its own failed to keep the  $\text{Cs}^+$  in solution and had no net effect on the  $[\text{Cs}^+]_{\text{ads}}$  due to  $\text{Cs}^+$  having a much higher affinity for the vermiculite (Kogure, 2012). To force this reaction forward and away from its natural equilibrium the  $\text{Cs}^+_{\text{aq}}$  would need to be captured and removed from the equilibrium so that more  $\text{Cs}^+$  could be displaced by the  $\text{Mg}^{2+}$  and the reaction can move forward. This results in a concerted desorption reaction and precipitation reaction that causes the net  $[\text{Cs}^+]_{\text{ads}}$  to decrease. This chemistry works because the  $\text{Cs}^+$  was removed from the solution and does not remain aqueous and was therefore unable to re-adsorb into the vermiculite interlayer.

This method worked well on the pure phase vermiculite, demonstrated some shortcomings when tested on Fukushima soil. The experimentation that followed looked to improve the method by increasing the efficiency and decreasing the cost of the treatment while testing reaction environments, looking into other possible precipitation agents, and establishing a mass balance of  $\text{Cs}^+$  once treated.

## 4.2 Materials and Methods

Pure phase vermiculite was purchased from VWR International, LLC (now Avantor) to create Cs-doped pure phase vermiculite. The pure phase vermiculite was mechanically ground and combined, ~40.00 g of the vermiculite was added to an Erlenmeyer flask to which 150 mL of a 0.05 M HCl (ACS Certified Plus) solution was added and allowed to mix on a mixing table overnight. This process was used to saturate the vermiculite with protons and desorb any other natively adsorbed ions that might be in the interlayer of the clay. The clay solids were filtered, and the supernatant was discarded. The acid-washed clay was combined and mixed to create a homogenous acid-washed pure phase vermiculite mixture. About 10.00 g of acid-washed pure phase vermiculite was added to an Erlenmeyer flask along with 100.00 mL of a 0.1M CsCl solution. This was allowed to mix with a stir bar for >48 hours. After the solution was allowed to reach equilibrium, the pH of the solution was measured. A 0.1 M solution of CsOH was added in 15 mL aliquots and allowed to mix overnight before checking the pH. This process was repeated until the pH reached a value above 9.5. The clay solids were then separated from the solution by vacuum filtration and rinsed with 20 mL of methanol and then 20 mL of deionized water. They were then placed in a scintillation vial. The process was repeated until enough Cs-doped pure phase vermiculite was gathered to complete the experimental procedure.

The extraction method that developed over the experimental process of this study started by adding  $0.500\text{g} \pm 0.005\text{ g}$  Cs-doped pure phase vermiculite into a 50 mL oak ridge centrifuge tube. Using a Metrohm 876 Dosimat Plus auto titrator 25.00 mL of 0.5M  $\text{Mg}(\text{NO}_3)_2$  certified ACS plus was added to the Cs-doped pure phase vermiculite in the centrifuge tube. Using an Eppendorf Repeater E3, 7 mL of 0.01 M precipitating counter ion (TFPB, PTA, MVPA, or STA) was added to the solution in the centrifuge tube (Synthetic methods and characterization of POMs included in the



previous chapter). The pH of this solution was adjusted by adding up to 3.00 mL of 1.21 M HCl certified ACS plus. 0 – 3.00 mL of deionized water was added to the solution using the auto titrator to bring it up to a total volume of 35.00 mL. Samples were left on the hematology mixer to reach equilibrium for at least 60 hours. These trials were repeated in quadruplicate.

After mixing, the samples were centrifuged at 7,800 g for 10 minutes and the supernatant was removed for analysis. The sample was then vacuum filtered through Whatman 41 qualitative filter paper. The Buchner funnel with the filter paper and residue on it was then placed on a clean gooseneck flask. The residue was rinsed with 120 mL of methanol. This was done in three 40 mL aliquots. The methanol dissolved the precipitate with the extracted Cs<sup>+</sup>. This methanol solution was evaporated by ~ 50 % and transferred to the digestion vessel, where the methanol was fully evaporated before digestion. The residue was removed from the filter paper and prepared for digestion. The filter paper itself was retained and prepared for digestion. Before digestion, it was combusted in a semi-closed ramekin at 550°C for 8.5 hours using a muffle furnace. This caused the ashless filter paper to combust into volatile organic compounds, making the digestion process more manageable. The residue left in the ramekin was rinsed with methanol into a digestion container and allowed to evaporate before digestion. Essentially for each treatment, four separate samples were created: the treated sample (T), which represents the treated clay. The treatment solution (TS) which was from the 35.00 mL solution used in the treatment vessel; the precipitate (P) which was from the methanol rinse that held the precipitating agent Cs<sup>+</sup> compound, and the filter paper (FP), which will hold any residue that was not able to be scraped away. An untreated sample (UT) was also taken by measuring 0.5 g of Cs-doped pure phase vermiculite and digested as well.

The digestion process for these samples followed the “EPA method 3050b acid digestion of sediments, sludges, and soils” adapted use in an Environmental Express TKN Hotblock. The digestion vessels were 50 mL test tubes (digestion tubes) specifically designed for use with the Hotblock. The digestion tubes were topped with a reflux bulb allowing the samples to reflux without losing volume with a higher efficiency than a ribbed watch glass. To digest, the sample was placed in the digestion tube, 5 mL of both concentrated analytical grade nitric acid, and deionized water were also added to the digestion tube. This was allowed to reflux at  $95.0 \pm 5.0^{\circ}\text{C}$  for 15 minutes. Any brown smoke produced was noted. After this reflux 2.5 mL of nitric acid was added and again refluxed for 15 minutes  $95.0 \pm 5.0^{\circ}\text{C}$ . This step was repeated until no brown smoke was produced but with a minimum of 10 mL of nitric acid in total being added. If no brown smoke was forming after the 15 minute reflux, the samples were left to reflux for an additional 2 hours. The next phase of the reflux focused on oxidative digestion using 30% hydrogen peroxide. This part of the digestion began with 2.5 mL of 30% hydrogen peroxide is added to the digestion tubes, along with 2.5 mL of deionized water. The samples refluxed with the peroxide until effervescence stopped. After the effervescence subsided 30% hydrogen peroxide was added to the vessels in 0.5 mL aliquots and left to effervesce in a similar fashion to before. Once effervescence subsided, or a total 10 mL of hydrogen peroxide had been added to the digestion tube, the samples were left to reflux for 2 hours at  $95.0 \pm 5.0^{\circ}\text{C}$ . The samples were then allowed to cool and were then prepared for ICP by the addition of 5.0 mL of concentrated hydrochloric acid. The samples were then refluxed for 15 minutes at  $95.0 \pm 5.0^{\circ}\text{C}$ . The samples were filtered through Whatman 41 quantitative filter paper and were then diluted to a volume above 35.0 mL before the final volume was recorded.

Following the digestion and filtration the samples were further prepared for ICP by placing a 10 mL aliquot of digestate into a 15 mL conical tipped centrifuge tube. A calibration curve was made in a similar fashion to the previous two experimental sets with calibration points at 1 mM, 5 mM, 10 mM, and 15 mM, with a DI blank. Because of the range of concentrations for these samples the radial view was used when observing the intensity of  $\text{Cs}^+$ . The spectral window was set at 894.353 nm. The  $[\text{Cs}^+]$  in the digestate solution was recorded and used to calculate the extraction potential of each ligand. The extraction was completed for each precipitating agent in quadruplicate and the average values were used to establish the extraction potential of the POMs and the TFPB.

#### *4.3 Results*

The concentrations of  $\text{Cs}^+$  were converted to mmol of  $\text{Cs}^+$  to compare the data. This was completed by multiplying the concentration of the digestates by the volume. The data were most easily compared by viewing the extraction potential as a percentage of the untreated samples. Once the solutions had been normalized into mmol  $\text{Cs}^+$ , the samples were placed into two categories: untreated and treated. The untreated samples were used to identify a value for mmol of  $\text{Cs}^+$  per gram of clay for the  $\text{Cs}^+$  doped pure phase vermiculite. This value was then used to calculate how much  $\text{Cs}^+$  would have been in the treated clay before a treatment based on its mass. The treated category of data included the treated clay, and the recovered  $\text{Cs}^+$ , which is represented by the  $\text{Cs}^+$  recovered in the treatment process. This was initially meant to be represented by the precipitate from the methanol rinse. But during the experimental phase of this study,  $\text{Cs}^+$  precipitate was found as a residue on the filter paper, in the  $\text{Mg}(\text{NO}_3)_2$  treatment solution, and in the methanol solution. The data below is presented in chronological order of experimentation, and the method development changes that are made between each step to reach the final method are denoted.

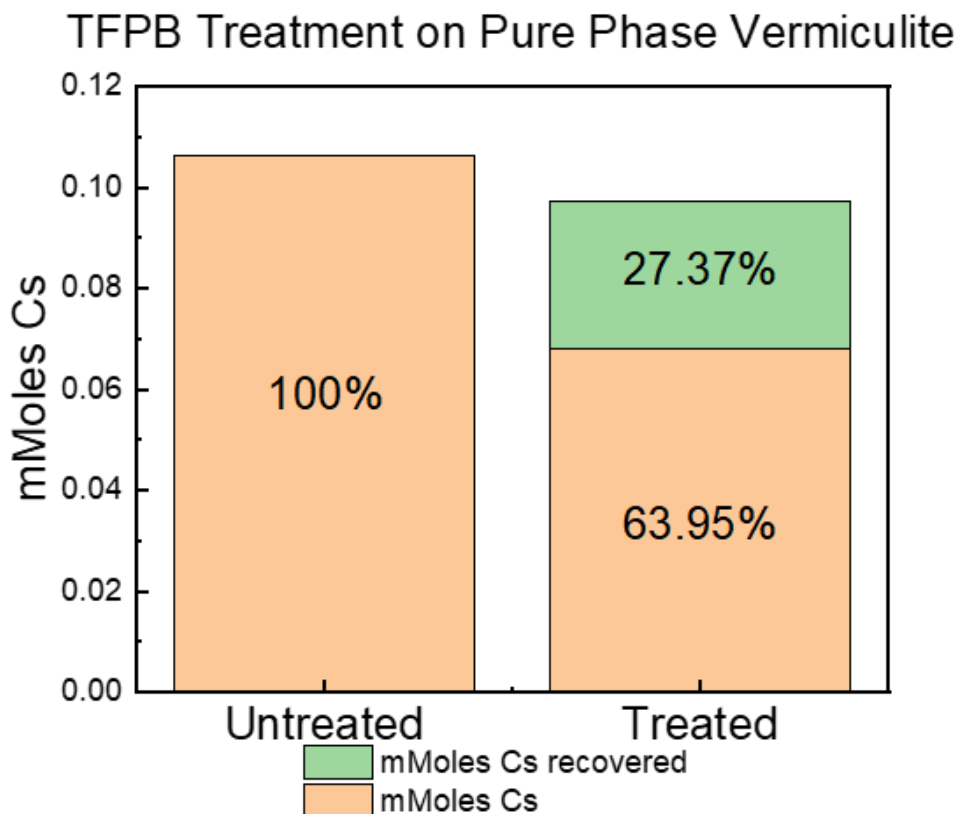


**Figure 4.1** Stacked bar graph of the extraction of  $\text{Cs}^+$  from doped pure phase vermiculite using TFPB. The orange section of the graph represents the amount of  $\text{Cs}^+$  in the clay. This value comes from digesting clay that has not been treated  $\sim 0.1089$  mmol of  $\text{Cs}^+$  for the untreated samples. The value represents the maximum amount of  $\text{Cs}^+$  for this trial, denoted by the 100% value on the graph. The amount of  $\text{Cs}^+$  left in the treated clay comes from analyzing the digestate of the treated clay. The green section of this figure is the resultant of the Cs recovered from the precipitate (P) that was digested.

When examining the treatment of the  $\text{Cs}^+$  doped pure phase vermiculite with TFPB (Figure 4.1), a total of 36.05% of the non-exchangeable  $\text{Cs}^+$  was able to be extracted from the clay, but only 27.37% of the  $\text{Cs}^+$  was able to be recovered. This yields a total mass balance of 91.32% which was higher than any other trial tested previously in the Ferreira lab.

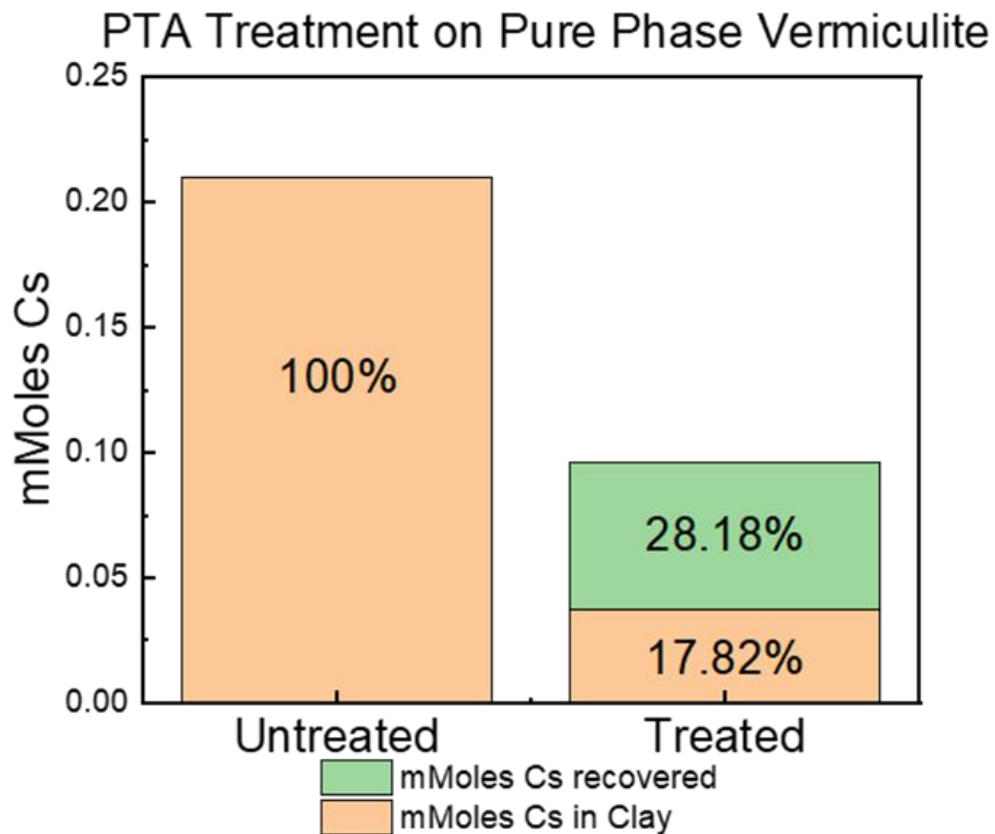


**Figure 4.2** Stacked bar graph of the extraction of  $\text{Cs}^+$  from doped pure phase vermiculite using PTA. This figure shows the amount of  $\text{Cs}^+$  in vermiculite represented by the orange sections of the graph. This includes the amount of cesium in the untreated clay  $\sim 0.2125$  mmol with the 100% value denotes this is the maximum value of  $\text{Cs}^+$  in the clay for this trial. The orange part of the graph for the treated clay indicates the amount of  $\text{Cs}^+$  left in the clay after treatment with the addition of the amount of  $\text{Cs}^+$ . The green section represents the amount of  $\text{Cs}^+$  recovered from only the P.

The PTA extraction process showed that the POM had a much higher extraction potential especially when compared to TFPB. This higher extraction potential was in line with the results from the speciation and stoichiometry trials. PTA was able to extract 82.18% of the  $\text{Cs}^+$  from the vermiculite. However only 28.18% of the  $\text{Cs}^+$  was recovered, which means only 49% of the mass balance was recovered. This led to an addition to the method going forward, as previously

mentioned, where an aliquot of the treatment solution was retained for analysis going forward as well as the filter paper. The reasoning behind retaining the treatment solution was that it might be possible for the POM to capture  $\text{Cs}^+$  but only become insoluble when their charge is fully neutralized.

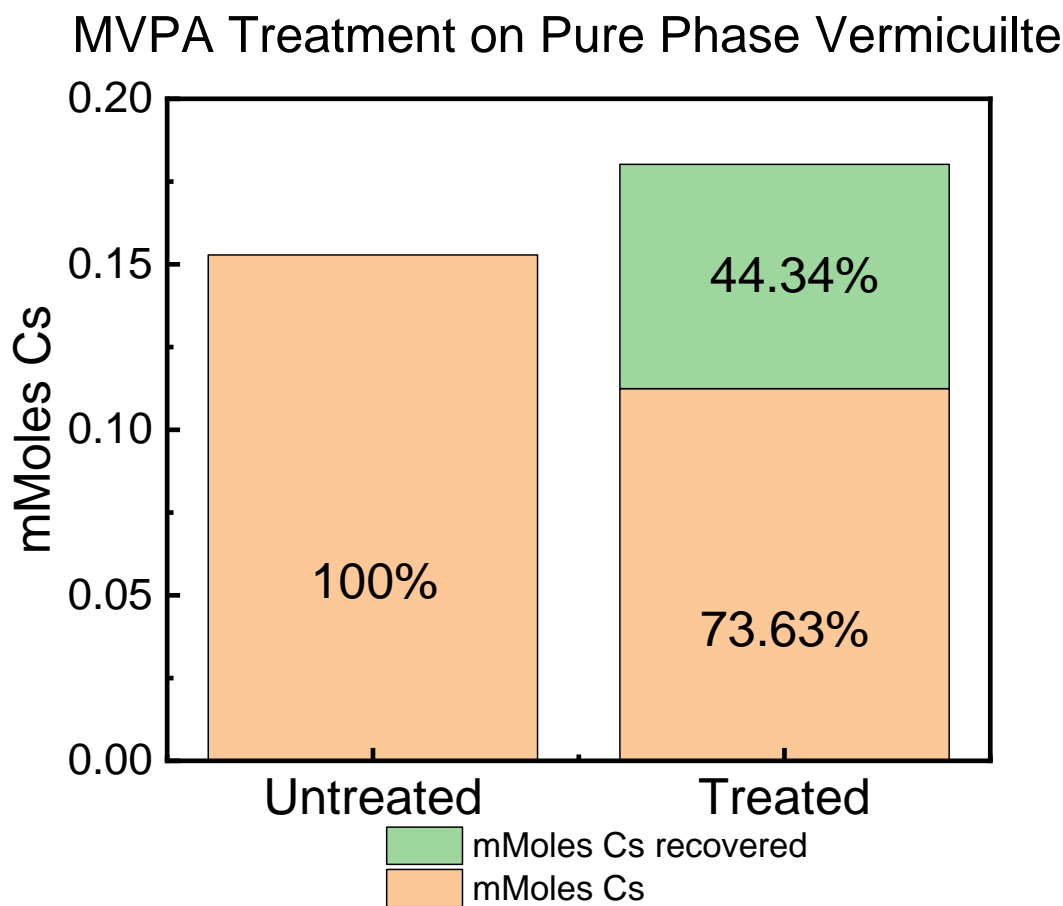


**Figure 4.3** Stacked bar graph of the extraction of  $\text{Cs}^+$  from doped pure phase vermiculite using MVPA. This graph represents the treatment results for MVPA after the addition of retaining the treatment solution and analyzing the filter paper was added to the method. The orange section of the graph represents the amount of  $\text{Cs}^+$  in the clay, the untreated sample around  $\sim 0.1508$  mmol of  $\text{Cs}^+$  per g which is the maximum amount of  $\text{Cs}^+$  for this trial denoted by the value 100%. The amount of  $\text{Cs}^+$  remaining for the treatment clay comes from the amount of  $\text{Cs}^+$  left in the clay and the amount of  $\text{Cs}^+$  on the FP. The recovered  $\text{Cs}^+$  represents the amount found in the P and the amount of  $\text{Cs}^+$  in the treatment solution.

The extraction with MVPA showed no real extraction potential advantage over using TFPB, although it is important to note that MVPA is a much cheaper precipitating agent, so if they are equal in extraction potential, MVPA is much more affordable. After the analysis of PTA, it was decided to try and analyze the treatment solution for Cs<sup>+</sup> after the filtration of the treatment solutions used for the MVPA extraction. One aliquot of the solution happened to have been retained. It was analyzed and the percentage Cs<sup>+</sup> found in the solution was applied to the other samples and included in the average. MVPA was able to extract only 26.37% of the Cs<sup>+</sup> from the vermiculite, but 117.97% was able to be recovered. If MVPA had a higher extraction potential, the series would have been repeated. However, because of the low extraction potential, a fourth precipitation agent was synthesized and tested.

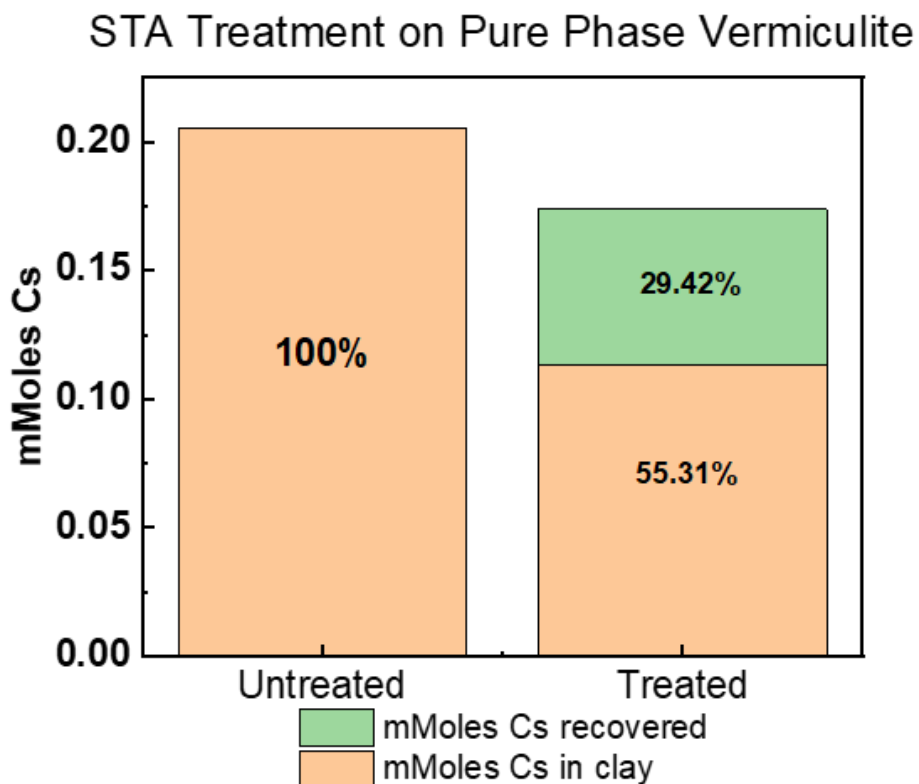


**Figure 4.4** Stacked bar graph of the extraction of Cs<sup>+</sup> from doped pure phase vermiculite using STA. The orange area of this graph represents the amount of Cs<sup>+</sup> found in vermiculite. For the UT

sample, the maximum value of  $\text{Cs}^+$  for this trial (denoted by the 100% value) was around 0.2001 mmol. The amount of  $\text{Cs}^+$  remaining in the treated clay represents the value from the analysis of both the treated clay and the FP. The amount of Cs denoted in green is the recovered fraction from this treatment. This value comes from an analysis of the P and the TS.

STA showed better extraction potential than MVPA and TFPB but failed to extract as much  $\text{Cs}^+$  as the PTA. However, with this extraction experiment, an aliquot of the treatment solution and the filter paper from the treatment was retained for each sample. STA was able to extract 44.69% of the  $\text{Cs}^+$  from the doped pure phase vermiculite while also allowing for 84.73% of the mass balance to be accounted for. It is also important to note that when looking at the data from the previous stoichiometry and speciation trials, STA had a higher extraction potential on a  $\text{Cs}^+$  per STA basis than PTA, and the concentration of STA was lower than the concentration of PTA in those trials, this could also be represented in the lower extraction potential shown here and could be due to a difference in purity between the synthesized STA and the purchased PTA.

When observing the extraction potential from the data of this experiment, there is clearly a difference between the POMs when comparing them to TFPB and themselves. PTA appears to have the highest extraction potential, but more experimentation is needed to try and find a reasonable mass balance with PTA. Also, further investigation could be completed with a purchased source of STA to ensure the experiment could be repeated with STA and PTA at equal concentrations verified by ICP.



## **CHAPTER 5. REMEDIATION METHOD FOR FUKUSHIMA SOIL**

### *5.1 Improvements & Optimal Conditions*

Through the experimental procedures presented in the previous chapters, the process of forcing the desorption of non-exchangeable  $\text{Cs}^+$  from vermiculite was much better understood. An updated extraction method is ready to be implemented on the actual soil from the Fukushima Daiichi Nuclear Powerplant area to remove radio  $\text{Cs}^+$  from the substrate.

The updated method for extraction of  $\text{Cs}^+$  from Fukushima soil that should be used for future research begins by preparing the soil for gravimetric separation by sieving through a 250-micron sieve to remove any large soil particles and detritus. The sieved soil should then be added to a solution of 5% sodium hexametaphosphate and allowed to equilibrate for at least 18 hours. This solution should be placed in a separatory column and diluted by bringing the solution up to one liter. This will equilibrate for at least 8 hours before stirring the solution should then be left to settle overnight. A peristaltic pump should extract the supernatant that contains the clay fraction of the soil. The sediment layer at the bottom will be left behind, and any detritus or organic matter floating on the top. The extracted clay will be dried by baking in a  $105^\circ\text{C}$  oven until all water has evaporated (~12 hours). The dried clay should then be placed in aluminum weigh boats and combusted by heating at  $550^\circ\text{C}$  for 8.5 hours in a muffle furnace. This will remove any remaining organic matter or hummin and leave only the clay fraction. The clay from multiple extractions should then be combined and ground with a mortar and pestle to form a homogenous mixture. Treating the clay starts by placing one gram of clay into a 50 mL nominal Oak Ridge centrifuge tube with 25.00 mL of 0.5M  $\text{Mg}(\text{NO}_3)_2$  (Certified ACS Grade), 7 mL of 0.02 M selective precipitation agent (TFPB, PTA, MVPA, or STA), and 3 mL of deionized water plus 1.2 M HCl this is used to adjust the pH and bring the final volume of the solution up to 35 mL in total. These

samples should be left to equilibrate on a hematology mixer for at least 60 hours to ensure all the possible precipitation agents have had time to precipitate out of the solution. The samples can then be filtered, and the precipitate removed from the residue by rinsing with methanol. According to the data gathered from experimentation on pure phase vermiculite the extracted  $\text{Cs}^+$  will be recovered in the methanol solution and in the  $\text{Mg}(\text{NO}_3)_2$  solution.

Improvements to this method were discovered throughout the entire experimental process of both the stoichiometry/speciation experiments and the extractions on pure phase vermiculite. The most critical improvements came from understanding the minimum time required for the precipitation to take place, and the speciation of the precipitation agents and tailoring the reaction environment to fit the POMs or the TFPB. These discoveries improved the extraction potential of the procedure. As far as fulfilling the mass balance and recovering the extracted  $\text{Cs}^+$  from the solution, discovering  $\text{Cs}^+$  (and precipitating agents) in the extraction solution was a huge step forward.

Demonstrating the efficacy of the POMs compared to TFPB also brings more cost-effective options for remediation to the table.

## *5.2 Concerns and limitations*

The Covid-19 pandemic of 2020, unfortunately, caused the supply of Fukushima soil to be unattainable. Experimentation is still under process to determine the efficacy of the extraction method on the natural soil, which is highly heterogeneous and may complicate the chemistry. Additionally, a serial application of the treatment method on the Fukushima soil could not be carried out to see how far the soil could be remediated. Another mitigating concern is the fact that the Cs-POM compounds seem to be more water soluble than previously thought when the POM charge is not fully neutralized. This is represented in the failure to reach a mass balance with PTA.

Another limitation is the lack of kinetic understanding of the precipitation of Cs-POM. Further experimentation may be required to fully understand the Cs-POM compounds in solution and the kinetics of the reaction.

### *5.3 Conclusion*

In conclusion, because of the loss of supply of Fukushima soil, we focused on the preliminary chemistry to better understand the flaws within the original remediation method. However, with further experimentation, and application of the final method developed from the experiments represented in this thesis, continued research on the Fukushima soil can take place with a better understanding, efficiency, and the possibility of reaching a mass balance of Cs<sup>+</sup> extracted to Cs<sup>+</sup> recovered.

## REFERENCES

1. Tamura, K.; Sato, H.; Yamagishi, A. Desorption of Cs<sup>+</sup> Ions from a Vermiculite by Exchanging with Mg<sup>2+</sup> Ions: Effects of Cs<sup>+</sup>-Capturing Ligand. *J. Radioanal. Nucl. Chem.*, **2015**, *303*, 2205-2210.
2. Nakao, A.; Ogasawara, S.; Sano, O.; Ito, T.; Yanai, J. Radiocesium sorption in relation to clay mineralogy of paddy soils in Fukushima, Japan. *Sci. Total Environ.*, **2014**, 468-469, 523-529.
3. Gaines Jr., G. L. The Ion-Exchange Properties of Muscovite Mica. *J. of P. Chem.*, **1957** *61* (10), 1408-1412.
4. Dolcater, D. L.; Jackson, M. L.; Syers, J. K. Cation Exchange Selectivity in Mica and Vermiculite. *Am. Mineral.*, **1972**, *57*, 1823-1831.
5. Perkins, H. F.; Tan, K.H. Potassium Fixation and Reconstitution of Micaceous Structures in Soils. *Soil Sci.*, **1973**, *116*(1), 31-35.
6. Sparks, D. L.; Zelazny, L. W.; Martens, D. C. Kinetics of Potassium Exchange in a Paleudult from the Coastal Plain of Virginia. *Soil Sci. Soc. Am. J.*, **1980**, *44*(1), 37-40.
7. Martin, H. W.; Sparks, D. L. On the Behavior of Nonexchangeable Potassium in Soils, *Comm. Soil Sci. Plan.*, **1985**, *16*:2, 133-162.
8. Sparks, D. L.; Carski, T. H. Kinetics of Potassium Exchange in Heterogeneous Systems. *Al. Clay Sci.*, **1985**, *1*, 89-101.
9. Sparks, D.L. Potassium Dynamics in Soils. *Advances in Soil Science*, **1987**, *6*.
10. Pal, D. K.; Durge, S. L. Release and Adsorption of Potassium in Some Benchmark Alluvial Soils of India in Relation to Their Mineralogy. *Pedologie*, **1989**, *39*(3), 235-248.

11. Osman, M. A.; Caseri, W. R.; and U.W. Suter. H<sup>+</sup>/Li<sup>+</sup> and H<sup>+</sup>/K<sup>+</sup> Exchange on Delaminated Muscovite Mica. *J. Colloid Interface Sci.*, **1998**, *198(1)*, 157-163.
12. Osman, M. A.; Moor, C.; Caseri, W. R.; Suter, U. W. Alkali Metals Ion Exchange on Muscovite Mica. *J. Colloid Interface Sci.*, **1999**, *209(1)*, 232-239.
13. Brady, N. C.; Weil, R. R. *The Nature and Properties of Soils*, 14th Edition. Pearson Education, 2008, Chapter 8.
14. Sato, K.; Fujimoto, K.; Dai, W.; Hunger, M. Molecular Mechanism of Heavily Adhesive Cs: Why Radioactive Cs is not Decontaminated from Soil. *J. Phys. Chem.*, **2013**, *117(27)*, 14075-14080.
15. Bostick, B. C.; Vairayamurthy, M. A.; Karthikeyan, K. G.; Chorover, J. Cesium Adsorption on Clay Minerals: An EXAFS Spectroscopic Investigation. *Environ. Sci. Technol.*, **2002**, *36*, 2670-2676.
16. Okumura, M.; Nakamura, H.; Machida, M. Mechanism of Strong Affinity of Clay Minerals to Radioactive Cesium: First-Principles Calculation Study for Adsorption of Cesium at Frayed Edge Sites in Muscovite. *J. Phys. Soc. Jpn.*, **2013**, *82 (3)*, 033802-033802-5.
17. Coleman, N. T.; Crag, D.; Lewis, R. J. Ion-exchange Reactions of Cesium. *Soil Sci. Soc. Am. J.*, **1963**, *27*, 287-289.
18. Huang, X.; Hu, S.; Wang, F.; Liu, Y.; Mu, Y. Properties of Alkali-Activated Slang with Addition of Cation Exchange Material. *Const. Built. Mater.*, **2017**; *146*, 321-328.
19. Yamamoto, T., Takigawa, T., Fujimura, T., Shimada, T., Ishida, T., Inoue, H., Takagi, S. Which Types of Clay Minerals Fix Cesium Ions Effectively? The “Cavity-Charge Matching Effect”. *Phys. Chem. Chem. Phys.*, **2019**, *21(18)*, 9352-9356.

20. Steinhauser, G. Fukushima's Forgotten Radionuclides: A Review of the Understudied Radioactive Emissions, *Environ. Sci. Technol.*, **2014**, *48*, 4649–4663, <https://doi.org/10.1021/es405654c>.
21. Tsubokura, M.; Nihei, M.; Sato, K.; Masaki, S.; Sakuma, Y.; Kato, S.; Sugimoto, A.; Nomura, S.; Matsumura, T.; Miyazaki, M.; Hayano, R.; Shibuya, K.; Kami, M.; Sasaki, T. Measurement of Internal Radiation Exposure Among Decontamination Workers in Villages Near the Crippled Fukushima Daiichi Nuclear Power Plant, *Health Phys.*, **2013**, *105*, 379–381, <https://doi.org/10.1097/HP.0b013e318297ad92>.
22. Tsubokura, M.; Kato, S.; Morita, T.; Nomura, S.; Kami, M.; Sakaiharu, K.; Hanai, T.; Oikawa, T.; Kanazawa, Y. Assessment of the Annual Additional Effective Doses Amongst Minamisoma Children during the Second Year after the Fukushima Daiichi Nuclear Power Plant Disaster, *PloS One*, **2015**, *10*, <https://doi.org/10.1371/journal.pone.0129114>.
23. Harada, K. H.; Niisoe, T.; Imanaka, M.; Takahashi, T.; Amako, K.; Fujii, Y.; Kanameishi, M.; Ohse, K.; Nakai, Y.; Nishikawa, T.; Saito, Y.; Sakamoto, H.; Ueyama, K.; Hisaki, K.; Ohara, E.; Inoue, T.; Yamamoto, K.; Matsuoka, Y.; Ohata, H.; Toshima, K.; Okada, A.; Sato, H.; Kuwamori, T.; Tani, H.; Suzuki, R.; Kashikura, M.; Nezu, M.; Miyachi, Y.; Arai, F.; Kuwamori, M.; Harada, S.; Ohmori, A.; Ishikawa, H.; Koizumi, A. Radiation Dose Rates Now and in the Future for Residents Neighboring Restricted Areas of the Fukushima Daiichi Nuclear Power Plant. *P. Natl. Acad. Sci. USA*, **2014**; *111*, 914–923, <https://doi.org/10.1073/pnas.1315684111>.

24. Yasutaka, T. and Naito, W.: Assessing Cost and Effectiveness of Radiation Decontamination in Fukushima Prefecture, Japan, *J. Environ. Radioactiv.*, **2016**, *151*, 512–520, <https://doi.org/10.1016/j.jenvrad.2015.05.012>.
25. Evrard, O.; Laceby, J. P.; Nakao, A. Effectiveness of Landscape Decontamination Following the Fukushima Nuclear Accident: A Review. *Soil*, **2019**, *5*, 333-350.
26. Cabrera, F.; Madrid, L.; De Arambarri, P. Adsorption of Phosphate by Various Oxides: Theoretical Treatment of the Adsorption Envelope. *J. Soil Sci.*, **1977**, *28*, 306-313.
27. McKenzie, R.M. The Adsorption of Molybdenum on Oxide Surfaces. *Aust. J. Soil Res.*, **1983**, *21(4)*, 505-513.
28. Sposito, G.; de Wit, J. C. M.; Neal, R. H. Selenite Adsorption on Alluvial Soils: III. Chemical Modeling. *Soil Sci. Soc. Am. J.*, **1988**, *52(4)*, 947-950.
29. Schulthess, C. P.; Huang, C.P. Humic and Fulvic Acid Adsorption by Silicon and Aluminum Oxide Surfaces on Clay Minerals. *Soil Sci. Soc. Am. J.*, **1991**, *55(1)*, 34-42.
30. Manning, B. A.; Goldberg, S. Modeling Competitive Adsorption of Arsenate with Phosphate and Molybdate on Oxide Minerals. *Soil Sci. Soc. Am. J.*, **1996**, *60*, 121-131.
31. Raven, K.P.; Jain, A.; Loeert, R. H. Arsenite and Arsenate Adsorption on Ferrihydrite: Kinetics, Equilibrium, and Adsorption Envelopes. *Environ. Sci. Technol.*, **1998**, *32(3)*, 344-349.
32. Arai, Y.; Sparks, D. L.Y.; Sparks, D. L. ATR–FTIR Spectroscopic Investigation on Phosphate Adsorption Mechanisms at the Ferrihydrite–Water Interface. *J. Colloid Interf. Sci.*, **2001**, *241(2)*, 317-326.
33. Lafferty, B. J., Loeert, R. H. Methyl Arsenic Adsorption and Desorption Behavior on Iron Oxides. *Environ. Sci. Technol.*, **2005**, *39 (7)*, 2120-2127.

34. Schulthess, C. P.; Taylor, R. W.; Ferreira, D.R. The Nanopore Inner Sphere Enhancement Effect on Cation Adsorption: Sodium and Nickel. *Soil Sci. Soc. Am. J.*, **2011**, 75(2), 378-388.
35. Ferreira, D. R.; Schulthess, C. P. The Nanopore Inner-Sphere Enhancement (NISE) Effect: Sodium, Potassium, and Calcium. *Soil Sci. Soc. Am. J.*, **2011**, 75(2), 389-396.
36. Song, W.; Justice, R. E.; Jones, C. A.; Grassian, V.H.; Larsen S.C. Synthesis, Characterization, and Adsorption Properties of Nanocrystalline ZSM-5. *Langmuir*, **2004**, 20, 8301-8306.
37. Baerlocher, C.; McCusker, L. B. *Database of zeolite structures*, **2021**, [https://america.iza-structure.org/IZA-SC/ftc\\_table.php](https://america.iza-structure.org/IZA-SC/ftc_table.php).
38. Flangan, D. M.; Crangle, Jr., R. D. Zeolites in Metals and Minerals., *USGS Minerals Yearbook*, v. 1, **2017**, 84, 1-84.4, <https://www.usgs.gov/centers/nmic/minerals-yearbook-metals-and-minerals>.
39. Ferreira, D. R.; Schulthess, C. P.; Giotto, M. V. An Investigation of Strong Sodium Retention Mechanisms in Nanopore Environments Using Nuclear Magnetic Resonance Spectroscopy. *Environ. Sci. Technol.*, **2012**, 46, 300-306.
40. Ferreira, D. R.; Schulthess, C. P.; Kabengi, N. J. Calorimetric Evidence in Support of the Nanopore Inner-Sphere Enhancement (NISE) Theory on Cation Adsorption. *Soil Sci. Soc. Am. J.*, **2013**, 77, 94-99.
41. Ferreira, D. R.; Thornhill, J. A.; Roderick, E. I. N.; Li, Y. The Impact of pH and Ion Exchange on <sup>133</sup>Cs Adsorption on Vermiculite. *J. Environ. Qual.*, **2018**, 47(6), 1365-1370.



42. Bleam, W. F. Adsorption and Surface Chemistry, Soil Environm. *Chem.*, **2012**, Ch. 9, 371-402.
43. Schulthess, C.P. *Soil Chemistry with Allied Mathematics*. Trafford Publ., Victoria, BC, Canada, **2005**.
44. Smith, D.W. Ionic hydration enthalpies. *J. Chem Educ.*, **1977**, 54(9), 540-542.
45. Rudziński, W.; Narkiewicz-Michalek, J.; Szabelski, P.; Chiang, A.S.T. Adsorption of Aromatics in Zeolites ZSM-5: A Thermodynamic-Calorimetric Study Based on the Model of Adsorption on Heterogeneous Adsorption Sites. *Langmuir*, **1997**, 13, 1095-1103.
46. Pulido, A.; Nachtigall, P.; Zukal, A.; Domínguez, I.; Čejka, J. *J. Phys. Chem.*, **2009**, 113, 2928-2935.
47. Kim, I.; Yang, H. M.; Park, C. W.; Yoon, I. H.; Seo, B. K.; Kim, E. K.; Ryu, B. G. Removal of Radioactive Cesium from an Aqueous Solution via Bioaccumulation by Microalgae and Magnetic Separation. *Sci. Rep.* **2019**, 9, 10149-10149.
48. Nakamura, A.; Sugawara, K.; Nakajima, S.; Murakami, K. Adsorption of Cs Ions Using a Temperature-Responsive Polymer/Magnetite/Zeolite Composite Adsorbent and Separation of the Adsorbent from Water Using High-Gradient Magnetic Separation. *Colloids Surf. A.* **2017**, 527, 63-69.
49. Sato, K.; Fujimoto, K.; Dai, W.; Hunger, M. Quantitative Elucidation of Cs Adsorption Sites in Clays: Toward Sophisticated Decontamination of Radioactive Cs. *J. Phys. Chem.*, **2016**, 120, 1270-1274.
50. Omori, T.; Sato, T.; Ishizuka, H.; Shiokawa, T. Reactions of Cs and Rb with Sodium Tetrakis(p-fluorophenyl)Borate. *J. Radioanal. Chem.* **1981**, 67, 299-306.

51. Saito, Y.; Shimizu, S.; Kumagai, S.; Kameda, T.; Yoshioka, T. Removal of Cesium Ions from A-type Zeolites Using Sodium Tetrakis(4-fluorophenyl)Borate and Sodium Tetraphenylborate. *J. Radioanal. Nucl. Chem.*, **2021**, 327.
52. Bajuk-Bogdanović, D.; Uskoković-Marković, S.; Holclajtner-Antunović, I. Vibration Spectroscopy STABILITY Investigation of 12-TUNGSTOSILICIC Acid Solution. *J. Iran Chem. Soc.*, **2014**, 12 (1), 137–145.
53. Pope, M. T. Heteropoly and Isopoly Oxometalates, *Springer-Verlag: Berlin*, **1983**.
54. Wang, S.-S., Yang, G.-Y. Recent Advances in Polyoxometalate-Catalyzed Reactions. *Chem. Rev.*, **2015**, 115, 4893-4962
55. Rhule, J. T.; Hill, C. L.; Judd, D. A.; Schinazi, R. F. Polyoxometalates in Medicine. *Chem. Rev.*, **1998**, 98, 327-358.
56. Keggin, J. F. The Structure and Formula of 12-Phosphotungstic Acid. *Proc. R. Soc. Lond. Ser. A* **1934**, 144, 75–100.
57. Liu, M.; Deng, W.; Zhang, Q.; Wang, Y.; Wang, Y. Polyoxometalate-supported ruthenium nanoparticles as bifunctional heterogeneous catalysts for the conversions of cellobiose and cellulose into sorbitol under mild conditions. *Chem. Commun.* **2011**, 47, 9717-9719.
58. Hiyoshi, N. Fabrication of Keggin-type Polyoxometalate Membranes at the Gas–Liquid Interface. *Langmuir*, **2020**, 36, 3958-3962.
59. Tsigdinos, G. A.; Hallada, C. J. Molybdovanadophosphoric Acids and Their Salts. I. Investigation of Methods of Preparation and Characterization. *Inorg. Chem.* **1968**, 7, 437-441.
60. Scroggie, A. G. Studies on Silcoduodecitungstic Acid. I. The Preparation of Silicotungstic Acid. *J. Am. Chem. Soc.*, **1929**, 51, 1057-1062.

61. Staiti, P. Proton Conductive Membranes Based on Silicotungstic Acid/Silica and Polybenzimidazole. *Mater. Lett.*, **2001**, *47*, 241-246.
62. Srikanth, A.; Viswanadham, B.; Kumar, V. P.; Anipindi, N. R.; Chary, K. V. R. Synthesis and Characterization of Cs-Exchanged Heteropolyacid Catalysts Functionalized with Sn for Carbonolysis of Glycerol to Glycerol Carbonate. *Al. Petrochem. Res.*, **2016**, *6*, 145-153.
63. Lua, S. K.; Oh, W.D.; Zhang, L.-Z.; Yao, L.; Lim, T.T.; Dong, Z. A Molybdovanadophosphate-Based Surfactant Encapsulated Heteropolyanion with Multi-Lamellar Nanostructure for Catalytic Wet Air Oxidation of Organic Pollutants Under Ambient Conditions. *RSC Adv.* **2015**, *5*, 94743-94751.
64. Purwanto, M.; Atmaja, L.; Mohamed, M. A.; Salleh, M. T.; Jaafar, J.; Ismail, A. F.; Santoso, M., Widiastuti, N. Biopolymer-Based Electrolyte Membranes from Chitosan Incorporated with Montmorillonite-Crosslinked GPTMS for Direct Methanol Fuel Cells. *RSC Adv.*, **2016**, *6*, 2314-2322.
65. Raveendra, G.; Rajasekhar, A.; Srinivas, M.; Sai Prasad, P. S.; Lingaiah, N. Selective Etherification of Hydroxymethylfurfural to Biofuel Additives Over Cs Containing Silicotungstic Acid Catalysts. *Al. Catal. A*, **2016**, *520*, 105-113.
66. Viswanadham, B.; Nekkala, N.; Rohitha, C.; Vishwanathan, V.; Chary, K. Synthesis, Characterization, and Catalytic Dehydration of Glycerol to Acrolein Over Phosphotungstic Acid Supported Y-Zeolite Catalysts. *Catal. Lett.* **2018**, 148.
67. Rair, D.; Aadad, H. E.; Jermoumi, T.; Chahine, A. Spectroscopic and thermal degradation studies of novel hybrid polymer based on sodium polyphosphate - polystyrene. *Mediterr. J. Chem.* **2018**, *7*, 337-345.

68. Parida, K. M.; Mallick, S. Hydroxylation of Phenol Over Molybdovanadophosphoric Acid Modified Zirconia. *J. Mol. Catal. A* **2008**, *279*, 104-111.
69. Viswanadham, B.; Srikanth, A.; Chary, K. V. R. Characterization and Reactivity of 11-Molybdo-1-vanadophosphoric Acid Catalyst Supported on Zirconia for Dehydration of Glycerol to Acrolein. *J. Chem. Sci.*, **2014**, *126*, 445-454.
70. Brahmkhatri, V.; Patel, A. Synthesis and Characterization of 12-Tungstosilicic Acid Anchored to MCM-41 as Well as Its Use as Environmentally Benign Catalyst for Synthesis of Succinate and Malonate Diesters. *Ind. Eng. Chem. Res.* **2011**, *50*, 13693-13702.
71. Berbeć, S.; Żołądek, S.; Kulesza, P. J.; Pałys, B. Silver Nanoparticles Stabilized by Polyoxotungstates. Influence of the Silver – Polyoxotungstate Molar Ratio on UV/Vis Spectra and SERS Characteristics. *J. Electroanal. Chem.*, **2019**, *854*, 113537.
72. Gao, L.-H.; Wang, K.-Z.; Wang, L.-Y. Self-assembled Films of a Biferrocenyl-containing Hemicyanine Derivative with SiW<sub>12</sub>O<sub>40</sub>(4-): Preparation, UV-visible Spectroscopy and Electrochemical Properties. *J. Nanosci. Nanotechnol.* **2010**, *10*, 2108-2112.
73. Chen, X.; Huang, P.; Zhu, X.; Zhuang, S.; Zhu, H.; Fu, J.; Nissimagoudar, A. S.; Li, W.; Zhang, X.; Zhou, L.; Wang, Y.; Lv, Z.; Zhou, Y.; Han, S.-T. Keggin-Type Polyoxometalate Cluster as an Active Component for Redox-Based Nonvolatile Memory. *Nanoscale Horiz.* **2019**; *4*, 697-704.
74. Cao, Y.-L.; Wang, L.; Bai, Y.-G.; Yan, R.-Y.; Xu, B.-H. Molybdovanadophosphoric Heteropolyacid-Catalyzed Aerobic Oxidation of Methacrolein: The Crucial Role of Ionic Liquid as a Modifier. *Catal. Lett.* **2020**; *150*, 1774-1785.

75. Chen, X.; Wang, H.; Xu, J.; Huo, M.; Jiang, Z.; Wang, X. Mixed Salts of Silver and Ammonium Derivatives of Molybdovanadophosphoric Acid to Improve the Catalytic Performance in the Oxidation of Starch. *Catal. Today*, **2014**, *234*, 264-270.
76. Scott J. E. Phosphotungstate: a "Universal" (Nonspecific) Precipitant for Polar Polymers in Acid Solution. *J Histochem Cytochem*, **1971**, *11*, 689-91. doi: 10.1177/19.11.689. PMID: 5121870.
77. Medvetskii, A. V.; Tikhomirova, T. I.; Tszin, G.I.; Dmitrienko, S. G.; Zolotov, Y. A. Sorption-Spectroscopic Determination of Phosphates in Waters as Molydenum Heteropoly Acids. *J. Analytic Chem.*, **2003**, *58 (9)*, 841-844.
78. Trakarnpruk, W.; Jatupisarnpong, J. Acidic and Cesium Salts of {olyxometalates with and without Vanadium Supported on MCM-41 as Catalysts for Oxidation of Cyclohexane with H<sub>2</sub>O<sub>2</sub>. *Al. Petrochem. Res.*, **2013**, *3*, 9-15.
79. Pesaresi, L.; Brown, D. R.; Lee, A. F.; Montero, J. M.; Williams, H.; Wilson, K. Cs-Doped H<sub>4</sub>SiW<sub>12</sub>O<sub>40</sub> Catalysts for Biodiesel Applications. *Al. Catal. A*, **2009**, *360*, 50-58.
80. Kuznetsova, L. I.; Detusheva, L. G.; Kuznetsova, N. I.; Koshcheev, S. V.; Zaikovskii, V. I.; Chesalov, Y. A.; Rogov, V. A.; Fenelonov, V. B.; Likholobov, V. A. Catalytic Properties of Platinum-promoted Acid Cesium Salts of Molybdophosphoric and Molybdovanadophosphoric Heteropoly Acids in the Gas-phase Oxidation of Benzene to Phenol with an O<sub>2</sub> + H<sub>2</sub> Mixture. *Kinet. Catal.* **2009**, *50*, 205-219.
81. Tanaka, K.; Takahashi, Y.; Sakaguchi, A.; Umeo, M.; Hayakawa, S.; Tanida, H.; Saito, T.; Kanai, Y. Vertical Profiles of Iodine-131 and Cesium 137 in Soil in Fukushima Prefecture Related to the Fukushima Daiichi Nuclear Power Station Accident. *Geoch. J.*, **2012**, *46*, 73-76.

82. Fuji, K.; Ikeda, S.; Akama, A.; Komatsu, M.; Takashi, M.; Kaneko, S. Vertical Migration of Radiocesium and Clay Mineral Composition in Five Forest Soils Contaminated by the Fukushima Nuclear Accident. *Soil Sci. Plant Nurt*, **2014**; *60*, 751-764.
83. Sawhney, B.L. Sorption and Fixation of Microquantities of Cesium by Clay Minerals: Effects of Saturating Cations. *Soil Sci. Soc. Am. J.*, **1964**, *28*(2), 183-186.
84. Lomenick, T. F., Tamura T. Naturally Occurring Fixation of Cesium-137 on Sediments of Lacustrine Origin. *Soil Soc. Sci. Am. J.*, **1965**, *29* (4), 383-387.
85. Sawhney, B.L. Selective Sorption and Fixation of Cations by Clay Minerals: A Review. *Clays Clay Miner.*, **1972**, *20*, 93-100.
86. Comans, R. N. J.; Hockley, D. E. Kinetics of Cesium Sorption on Illite. *Geochim. Cosmochim. Ac.*, **1992**, *56*, 1157-1164.
87. Missana, T.; Garcia-Gutierrez, M.; Alonso, U. Kinetics and Irreversibility of Cesium and Uranium Sorption onto Bentonite Colloids in a Deep Granitic Environment. *Al. Clay Sci.*, **2004**, *26*, 137-150.
88. Iijima, K.; Tomura, T.; Shoji, Y. Reversibility and Modeling of Adsorption Behavior of Cesium Ions on Colloidal Montmorillonite Particles. *Al. Clay. Sci.*, **2010**, *49*, 262-268.
89. Kogure, T.; Morimoto, K.; Tamura, K.; Sato, H.; Yamagishi, A. XRD and HRTEM Evidence for Fixation of Cesium Ions in Vermiculite Clay. *Chem. Lett.*, **2012**, *41*, 380-382.
90. Dzene, L.; Tertre, E.; Hubert, F.; Ferrage, E. Nature of the Sites Involved in the Process of Cesium Desorption from Vermiculite. *J. Colloid Interf. Sci.*, **2015**, *455*, 254-260.

91. Fuller, A. J.; Shaw, S.; Ward, M. B.; Haigh, S. J.; Mosselmans, J. F. W.; Peacock, C. L.; Stackhouse, S.; Dent, A. J.; Trivedi, D.; Burke, I. T. Cesium Incorporation and Retention in Illite Interlayers. *Al. Clay Sci.*, **2015**, *108*, 128-134.